NATIONAL ENERGY TECHNOLOGY LABORATORY

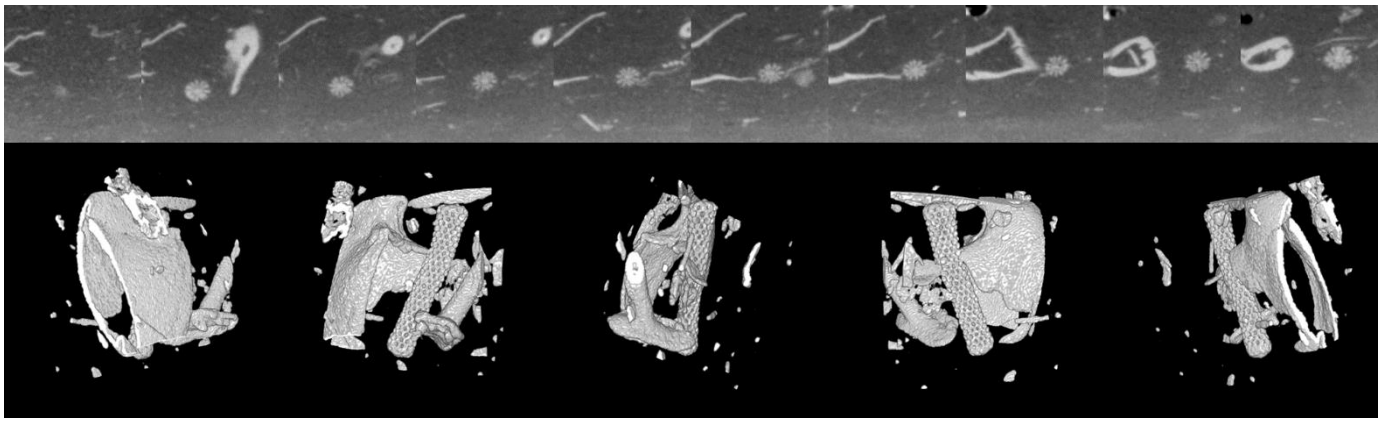

Computed Tomography Scanning and Geophysical Measurements of the Integrated Mid-Continent Stacked Carbon Storage Hub Sleepy Hollow Reagan Unit 86A Well

15 September 2024

U.S. DEPARTMENT OF ENERGY | NATIONAL ENERGY TECHNOLOGY LABORATORY

Office of Fossil Energy and Carbon Management

DOE/NETL-2024/4808

Disclaimer

This project was funded by the United States Department of Energy, National Energy Technology Laboratory, in part, through a site support contract.

Cover Illustration: Industrial computed tomography (CT) montage and three-dimensional (3D) segmentation of the Integrated Mid-Continent Stacked Carbon Storage Hub Sleepy Hollow Reagan Unit 86A (IMSCS-HUB SHRU 86A) well at 2,906 to 2,909 ft; fossils include bryozoan stems, brachiopod (partial, upper and lower valves), and fossil fragments.

Suggested Citation: Paronish, T.; Pohl, M.; Parker, A.; Tempke, R.; Moore, J.; Spaulding, R.; Haljasmaa, I.; Crandall, D.; Smith, V.; Duguid, A.; Joeckel, R. M. *Computed Tomography Scanning and Geophysical Measurements of the Integrated Mid-Continent Stacked Carbon Storage Hub Sleepy Hollow Reagan Unit 86A Well;* DOE/NETL-2024/4808; NETL Technical Report Series; U.S. Department of Energy, National Energy Technology Laboratory: Morgantown, WV, 2024; p 60. DOI: 10.2172/2446569.

An electronic version of this report can be found at:

https://netl.doe.gov/energy-analysis/search

https://edx.netl.doe.gov/group/core-characterization

The data in this report can be accessed from NETL's Energy Data eXchange (EDX) online system (https://edx.netl.doe.gov) using the following link: https://edx.netl.doe.gov/dataset/IMSCS-HUB_SHRU_86A_Core

Computed Tomography Scanning and Geophysical Measurements of the Integrated Mid-Continent Stacked Carbon Storage Hub Sleepy Hollow Reagan Unit 86A Well

Thomas Paronish[1,3]; Mathias Pohl[1,3]; Alexis Parker[1,2]; Rhiannon (Schmitt) Tempke[1,3]; Johnathan Moore[1,3]; Richard Spaulding[1]; Igor Haljasmaa[1,3]; Dustin Crandall[1]; Valarie Smith[4]; Andrew Duguid[4,5]; R. M. Joeckel[6]

[1]National Energy Technology Laboratory, 3610 Collins Ferry Road, Morgantown, WV 26505, USA

[2]Mickey Leland Energy Fellowship, 3610 Collins Ferry Road, Morgantown, WV 26505, USA

[3]NETL Support Contractor, 3610 Collins Ferry Road, Morgantown, WV 26505, USA

[4]Battelle Memorial Institute, 505 King Avenue, Columbus, Ohio 43201, USA

[5]Advanced Resources international, 1840 Mackenzie Drive, Suite 100, Columbus, Ohio 43220, USA

[6]Conservation and Survey Division, School of Natural Resources, University of Nebraska-Lincoln, 615 Hardin Hall, Lincoln, NE 68583, USA

DOE/NETL-2024/4808

15 September 2024

NETL Contacts:

Dustin Crandall, Principal Investigator

Colton Kohnke, Technical Portfolio Lead

Bryan Morreale, Associate Laboratory Director for Research & Innovation Center, Research & Innovation Center

This page intentionally left blank.

Table of Contents

List of Figures

List of Figures (cont.)

List of Tables

Acronyms, Abbreviations, and Symbols

Term	Description
2D	Two-dimensional
3D	Three-dimensional
CO_2	Carbon dioxide
CT	Computed tomography
CTN	Computed tomography number
DOE	U.S. Department of Energy
EDX	NETL's Energy Data eXchange
H	External magnetic field
HU	Hounsfield Unit
IMSCS-HUB SHRU 86A	Integrated Mid-continent Stacked Carbon Storage Hub Sleepy Hollow Reagan Unit 86A
J	Magnetic response
k	Volume susceptibility
MSCL	Multi-Sensor Core Logger
NETL	National Energy Technology Laboratory
ρ_B	Density
PDP	Pulse Decay Permeameter-200
SHF	Sleepy Hallow Field
SHRU	Sleepy Hallow Reagan Unit
XRF	X-ray fluorescence
Z	Acoustic impedance

Acknowledgments

This work was performed in support of the National Energy Technology Laboratory's (NETL) ongoing research under the Office of Carbon Management Program by NETL's Research and Innovation Center. The authors wish to acknowledge Bryan Morreale and Ale Hakala (NETL Research & Innovation Center), Mark McKoy (NETL Science and Technology Strategic Plans and Programs), and Darin Damiani (DOE Office of Carbon Management) for programmatic guidance, direction, and support.

The authors would like to thank Bryan Tennant and Scott Workman for data collection and technical support. This research was supported in part by appointments from the NETL Research Participation Program, sponsored by the U.S. DOE and the Mickey Leland Energy Fellowship and administered by the Oak Ridge Institute for Science and Education.

ABSTRACT

The computed tomography (CT) facilities, the Multi-Sensor Core Logger (MSCL), and the Geologic Storage Core Flow Laboratory at the National Energy Technology Laboratory (NETL) in Morgantown, West Virginia and Pittsburgh, Pennsylvania were used to characterize a core through Upper Pennsylvanian strata (limestones, mudstones, and sandstones) from the Sleepy Hollow Reagan Unit (SHRU) 86A well in southwest-central Nebraska. The Integrated Mid-Continent Stack Carbon Storage Hub (IMSCS-HUB) core from the vertical well was obtained as part of the U.S. Department of Energy's (DOE) effort to assess the feasibility of stacked storage complexes in Nebraska and Kansas to support a commercial-scale CO_2 storage hub. The Sleepy Hollow Field (SHF) is one of three sites within the IMSCS-HUB corridor. Bulk scans of core were obtained from the IMSCS-HUB SHRU 86A well. This report, and the associated scans, include detailed datasets not typically made available to the public. The datasets presented in this report can be accessed from NETL's Energy Data eXchange (EDX) online system using the following link: https://edx.netl.doe.gov/dataset/IMSCS-HUB_SHRU_86A_Core.

All equipment and techniques used in producing the data for this report are non-destructive and will not hamper future examinations and analyses of the SHRU 86A core. Micro-CT scanning captured sub-millimeter-scaled pores in sandstone along with fractures and discontinuities that went undetectable by other methods. Low-resolution CT imagery with the NETL medical CT scanner was also performed on the entire core. Qualitative analysis of the medical CT images, coupled with X-ray fluorescence (XRF), P-wave, and magnetic susceptibility measurements from the MSCL, helped to identify fractured zones and other zones of interest for more detailed analyses. If implemented, this approach of rapidly identifying parts of a core for more detailed study at higher resolutions will save time and resources in future core studies. In another phase of this work, the industrial CT scanner was used to create higher resolution scans of core. Porosity, permeability, and mechanical properties of sub-cores were performed to enhance the understanding of various formations intersected by the SHRU 86A core for subsurface engineered applications. The combination of methods used provided a multi-scale analysis of this core and an industrial, macroscale, and microscale description of the core that should be highly applicable in many of the subsurface energy-related research programs traditionally performed at NETL.

1. INTRODUCTION

The evaluation of reservoir samples supports resource estimation and the determination of effective injection methodologies. Although it is common for commercial entities to perform these characterizations, state agencies, universities, and research-based consortiums frequently lack the necessary resources. To meet the growing need for comprehensive and high-quality lithologic data for collaborative research initiatives, the U.S. Department of Energy's (DOE) National Energy Technology Laboratory (NETL) has used available resources in conjunction with proven techniques and new, innovative methodologies to develop a systematic approach for the evaluation of cores. This report focuses on the Integrated Mid-Continent Stack Carbon Storage Hub (IMSCS-HUB) Sleepy Hollow Reagan Unit (SHRU) 86A well.

IMSCS-HUB SHRU 86A well was drilled in the summer of 2019 in the Sleepy Hollow Field (SHF), in Red Willow County, southwest-central Nebraska. The SHF is approximately 28 mi^2 and is the most productive oil field in Nebraska having produced over 48 million barrels of oil primarily from the basal Pennsylvanian Sandstone (Bacon et al., 2018). The field consists of a northeast-southwest trending anticlinal structure located on the southwestern flank of a buried, gentle structural feature of typical cratonic affinities, the Cambridge Arch (Bacon et al., 2018).

Permeable and porous Paleozoic deep saline carbonate formations have been identified as potential geologic storage complexes in the SHF. The focus of the DOE-funded CarbonSAFE project (Duguid, 2017) was the identification of deep saline CO_2 storage and an evaluation of the four main lithostratigraphic groups of the Pennsylvanian System in the southwest-central area, namely:

- Porous limestones of the Pleasanton and Marmaton groups (lower Core 4)
- Strata of the combined Lansing–Kansas City groups (upper Core 4)
- Sandstone intervals in the Shawnee and Douglas groups (Core 3) as well as the overlying Wabaunsee Group (Core 2)

All permeable and porous beds are overlain by a mudrock seal in the form of the Upper Pennsylvanian–Lower Permian Admire Group (Core 1).

1.1 STUDY AREA

The study area for the IMSCS-HUB SHRU 86A well is the SHF located in Red Willow County, southwest-central Nebraska. The well was drilled, cored, and logged in May and June 2019. The IMSCS-HUB was comprised of carbon dioxide (CO_2) sources in Iowa, Kansas, and Nebraska, and CO_2 sinks in Kansas and Nebraska. Other potential sinks in this region are described in Paronish et al. (2022a, 2022b) and Schmitt et al. (2022). Figure 1 shows the site location and IMSCS-HUB corridor. The SHF is one of three CO_2 sinks characterized by six alternating sequences of deep saline formations, oil-bearing reservoirs, shale, and evaporite units (Smith, 2022). Photos for the cored sections are represented in Figures 2 to 9.

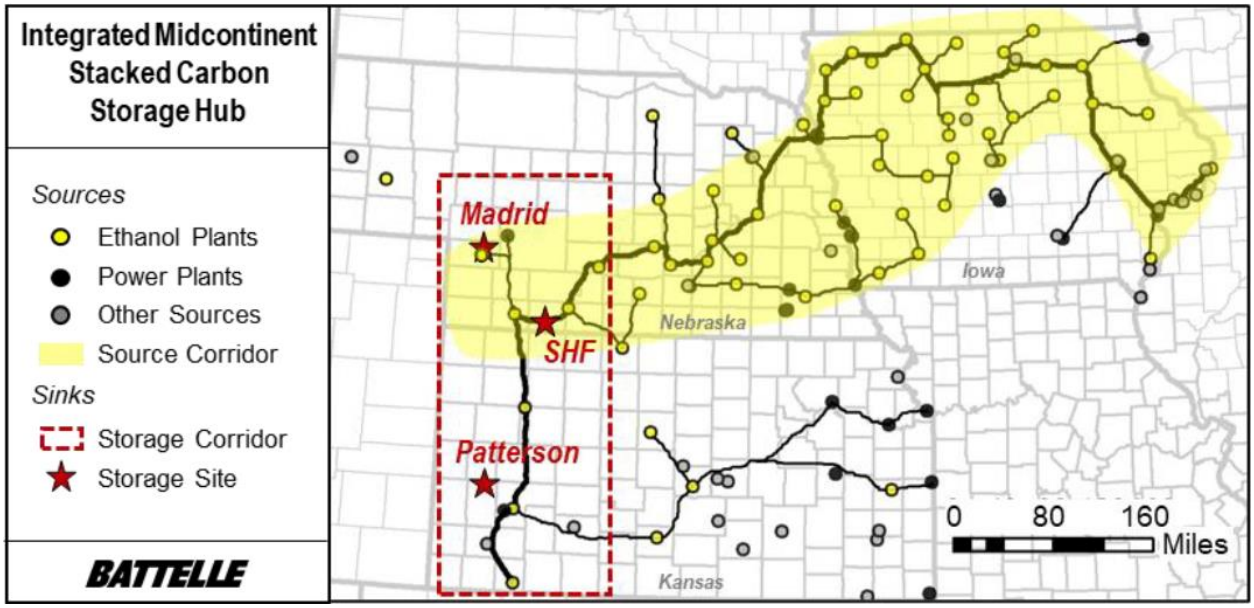

Figure 1: The three site locations for the IMSCS-HUB, including the SHF in southwestern Nebraska.

1.2 CORE PHOTOGRAPHS

Figure 2: Core 1 from the IMSCS-HUB SHRU 86A well, depth 2,900-2,918 ft. Scale (middle) is in feet and tenths of feet.

Figure 3: Core 1 from the IMSCS-HUB SHRU 86A well, depth 2,918-2,931 ft. Scale (middle) is in feet and tenths of feet.

Figure 4: Core 2 from the IMSCS-HUB SHRU 86A well, depth 3,009-3,027 ft. Scale (middle) is in feet and tenths of feet.

Figure 5: Core 2 from the IMSCS-HUB SHRU 86A well, depth 3,027-3,038.65 ft. Scale (middle) is in feet and tenths of feet.

Figure 6: Core 3 from the IMSCS-HUB SHRU 86A well, depth 3,161-3,179 ft. Scale (middle) is in feet and tenths of feet.

Figure 7: Core 3 from the IMSCS-HUB SHRU 86A well, depth 3,179-3,190.85 ft. Scale (middle) is in feet and tenths of feet.

Figure 8: Core 4 from the IMSCS-HUB SHRU 86A well, depth 3,479-3,497 ft. Scale (middle) is in feet and tenths of feet.

Figure 9: Core 4 from the IMSCS-HUB SHRU 86A well, depth 3,497-3,501.85 ft. Scale (middle) is in feet and tenths of feet.

2. DATA ACQUISITION AND METHODOLOGY

The 2/3rd slabbed core was evaluated using computed tomography (CT) scanning and traditional core logging.

2.1 CORE LOGGING

Geophysical measurements of core thickness deviation, P-wave travel time, magnetic susceptibility, and attenuated gamma counts can be obtained with a Geotek® Multi-Sensor Core Logging (MSCL, Figure 10) system on a competent core. The P-wave velocity was measured for the scanned 2/3rd slabbed core. Bulk elemental chemistry was also measured with a built-in, portable X-ray fluorescence (XRF) spectrometer. For a full description of the MSCL capabilities at NETL, please see Crandall et al. (2017).

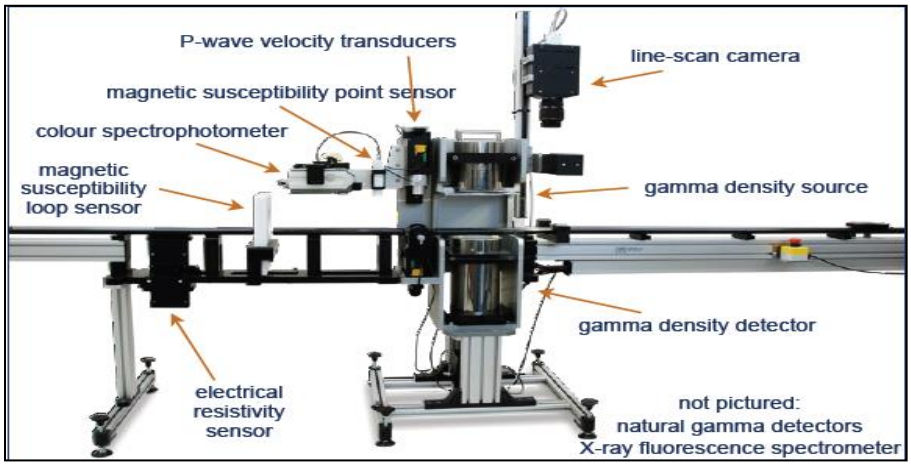

Figure 10: Representation of generalized MSCL with all attached instruments. From Geotek Ltd., Geotek Multi-Sensor Core Logger Flyer, Daventry, UK (2009).

2.1.1 Magnetic Susceptibility

Magnetic susceptibility is a measure of the degree of magnetization in a sample. A sample is exposed to an external magnetic field and the magnetic response of the sample is measured:

$$J = kH$$

Where J is the magnetic response (per unit volume), k is volume susceptibility, and H is an external magnetic field. The measurement unit is dimensionless (abbreviated simply as SI). All materials have magnetic susceptibility. Positive values of magnetic susceptibility indicate that materials are paramagnetic and occur in rocks that are comprised of the majority ferromagnetic, ferrimagnetic, or antimagnetic (iron bearing) materials. Whereas negative values of magnetic susceptibility indicate that materials are diamagnetic. Rocks dominated by non-iron-bearing minerals, such as calcite or quartz, exhibit negative values. Table 1 lists examples of common ranges of magnetic susceptibility in water and minerals that are common or relatively common in sediments and sedimentary rocks (Hunts et al., 1995).

Magnetic susceptibility is measured using the Bartington point sensor, where a 1 cm diameter, low intensity (8.0 A/m RMS), non-sensitive, alternating magnetic field (2 kHz) is generated for 10 seconds. To minimize any potential drift in the oscillating field the point sensor is zeroed at the beginning and end of the sample, as well as, after every fifth measurement. The point sensor, due to the small field, is limited in whole core measurements, and is temperature dependent (Geotek Ltd. Multi-Sensor Core Logger Manual, Version 05-10; Geotek Ltd., 2010).

Table 1: Magnetic Susceptibility Values for Common Minerals (Hunts et al., 1995)

Mineral	x (*10^{-6}) SI
Water	9
Calcite	-7.5 to -39
Halite, Gypsum	-10 to -60
Shale	63 to 18,600
Illite, Montmorillonite	330 to 410
Pyrite	5 to 3,500
Chalcopyrite	23 to 400
Hematite	500 to 40,000
Magnetite	1,000,000 to 5,700,000

2.1.2 P-wave Velocity

P-wave velocity measurements quantify the acoustic impedance of a geologic material subjected to compressional waves. Acoustic impedance (Z) is a measure of how well a material transmits vibrations, which is directly proportional to its density (ρ_B) and/or consolidation:

$$Z = v * \rho_B$$

Where v is wave velocity. In the example of air, a gas with negligible density and stiffness in comparison with solid Earth materials has low acoustic impedance and transmits compressional waves at 330 m/s. Granite, in contrast, has a high acoustic impedance and transmits compressional waves rapidly at >5,000 m/s. Measurements of P-wave velocity can be proxies for seismic reflection coefficients and are translatable for field use in seismic surveys.

The software used in the MSCL measures the travel time of a pulse with a resolution of 50 ns. The absolute accuracy of the instrument measurements is $\pm$ 3 m/s with a resolution of 1.5 m/s (Geotek Ltd. Multi-Sensor Core Logger Manual, Version 05-10; Geotek Ltd., 2010).

2.1.3 X-Ray Fluorescence Spectrometry

In addition to the geophysical measurements, a portable handheld Innov-X® X-Ray Fluorescence Spectrometer was used to measure relative elemental abundances of aggregated “light” elements on the periodic table (green-shaded elements in Figure 11), up to and including sodium (Na).

Various heavy elements were also measured, albeit individually (Figure 11). Elemental abundances are reported relative to the total elemental composition, which is, out of 100% weight.

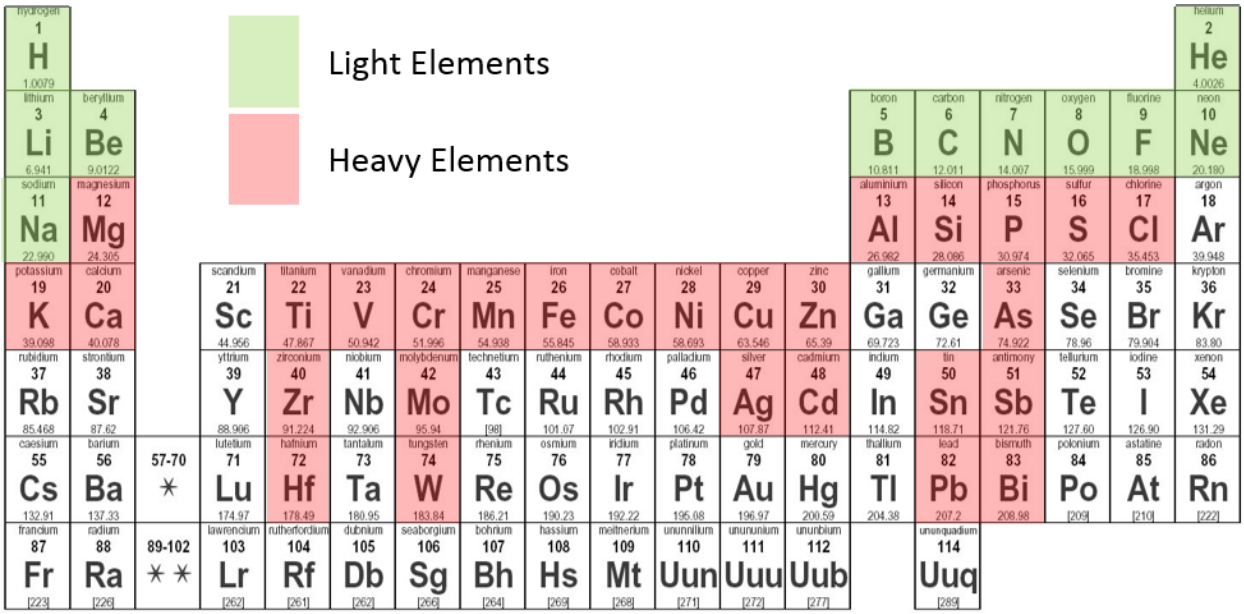

Figure 11: Periodic table showing elements measurable by the Innov-X® X-Ray Fluorescence Spectrometer (shaded).

The XRF spectrometer measures elemental abundances by subjecting the sample to X-ray photons. The high energy of the photons displaces inner-orbital electrons in atoms of the respective elements. The vacancies in the lower orbitals cause outer orbital electrons in an atom to "fall" into lower orbits, thus satisfying the disturbed electron configuration. The substitution of electrons into lower orbitals releases energy in the form of a secondary X-ray photon, which has an energy associated with a specific element. These relative and element specific energy emissions can then be used to determine bulk elemental composition.

2.2 MEDICAL CT SCANNING

Core scale CT scanning was performed with a Toshiba® Aquilion TSX-101A/R medical scanner as shown in Figure 12. The medical CT scanner generates images with a resolution in the millimeter range, with scans having voxel resolutions of 0.43 x 0.43 mm in the XY plane and 0.50 mm along the core axis. The scans were conducted at a voltage of 135 kV and at 200 mA. Subsequent processing and combining of stacks was performed to create three-dimensional (3D) volumetric representations of the cores and a two-dimensional (2D) cross-section through the middle of the core samples using ImageJ (Schneider et al., 2012). The variation in greyscale values observed in the images indicates changes in the CT number (CTN) obtained from the scans, which is directly proportional to changes in the attenuation and density of the scanned rock, i.e., darker regions are less dense. As can be seen in Section 3, filled fractures, open fractures, and changes in bedding structure can be resolved via careful examination of the CT images. While the medical CT scanner was not used for detailed characterization in this study, it allowed for non-destructive bulk characterization of the core, and thus complimented the MSCL data on the resultant logs.

Figure 12: Toshiba® Aquilion™ TSX-101A/R medical scanner at NETL used for core analysis.

2.3 INDUSTRIAL CT SCANNING

Detailed scans of a section of interest (please refer to Section 4.3) were performed using the NorthStar Imaging Inc. M-5000® Industrial Computed Tomography System (Industrial CT) at NETL (Figure 13). The system was used to obtain higher resolution scans with variable voxel resolution between 20.1 and 100.4 μm3 (Table 2) and capture the details of certain features clearly. The scan on sections of the whole core were performed at a voltage of 185 kV and a current of 400 μA, and scans of core plugs were performed at 185kV and 200 μA. These settings provided the proper photon energy to penetrate the samples. The samples were rotated 360° and 1,440 radiograph projections of the samples were obtained, averaging 12 individual radiographs at each step to create the reconstruction.

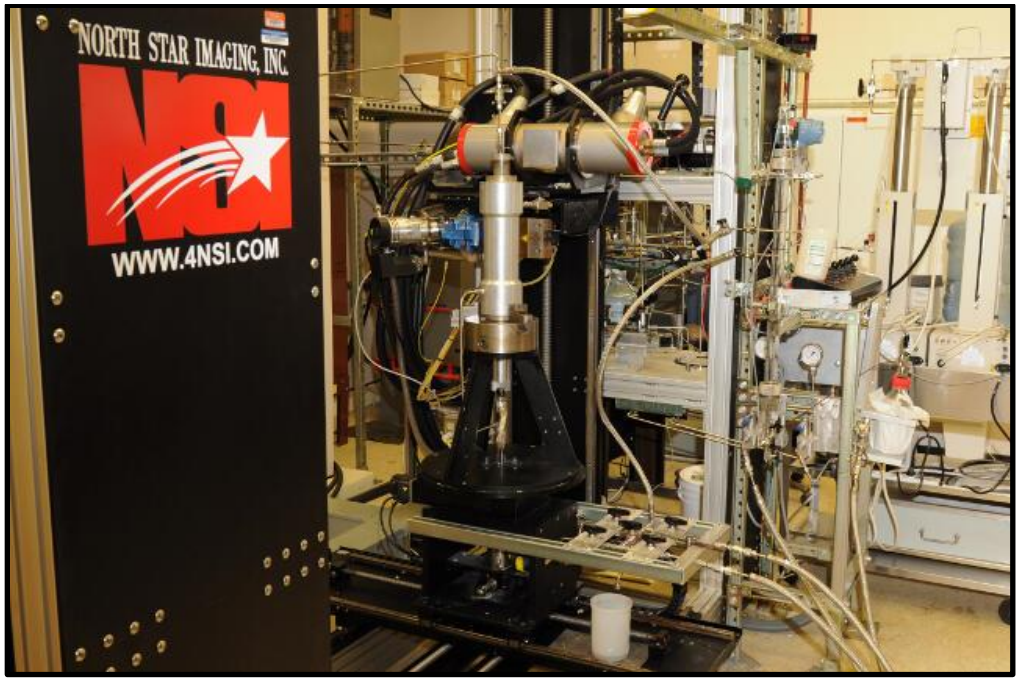

Figure 13: North Star Imaging Inc. M-5000 ® Industrial CT Scanner at NETL used for core analysis.

2.4 MICRO-CT SCANNING

Micro-CT scanning was acquired using the ZEISS Xradia micro-CT scanner. The ZEISS Xradia micro-CT scanner has the highest resolution of the scanners at NETL and scans samples sized from sub-mm to 25 mm and provides detailed data on porosity, mineralogy, and structure.

2.5 POROSITY, PERMEABILITY, AND GEOMECHANICAL MEASUREMENTS

Porosity for all the cores was measured by a helium porosimeter, HP-401 (TEMCO, Inc.) (Figure 14). This device uses helium gas to penetrate the pores of the core sample in a closed system at a pressure of several atmospheres. The measurements for this study were made at both confining and pore pressures of roughly 75–85 psi. Porosity was then calculated using Boyle's law and a steel reference core of known volume. It is important to remember that the reported porosity values may somewhat underestimate porosity at depth, especially for compliant pores that may partially close under high lithostatic pressures.

Figure 14: Helium porosimeter HP 401 (TEMCO, Inc.).

Two permeameters were utilized for permeability measurements of the cores (Figure 15). The TEMCO/CoreLabs UltraPerm-500 device is a constant-flow nitrogen permeameter, which calculates permeability from the generated pressure difference and the resultant measured flow rate of gas. Due to its low range of pore pressures (1–4 atm), this device has limited applicability for tight stratigraphic intervals with smaller pores and/or lower values of porosity. At the same time, it can confine the samples, allowing determination of permeability as a function of lithological compression. Low pore pressures also cause "slippage" of the gas molecules in the pore space (the so called "Klinkenberg effect"), overestimating permeability of the cores compared to the "true" or "liquid" permeability. For the correction of this effect, several measurements were performed at different pore pressures, and the "true" permeability was obtained as an extrapolation to the infinite pore pressure. For the tight cores that have permeability an order of or below 0.01 mD, the TEMCO/CoreLab Pulse Decay Permeameter-200 (PDP) was used. The PDP utilizes a transient method, where a pressure step is generated on one end of the sample. Permeability is then derived from the measured pressure response on the other end. Since the operational pressure on the pore side is several hundred psi, no Klinkenberg correction is required for this device.

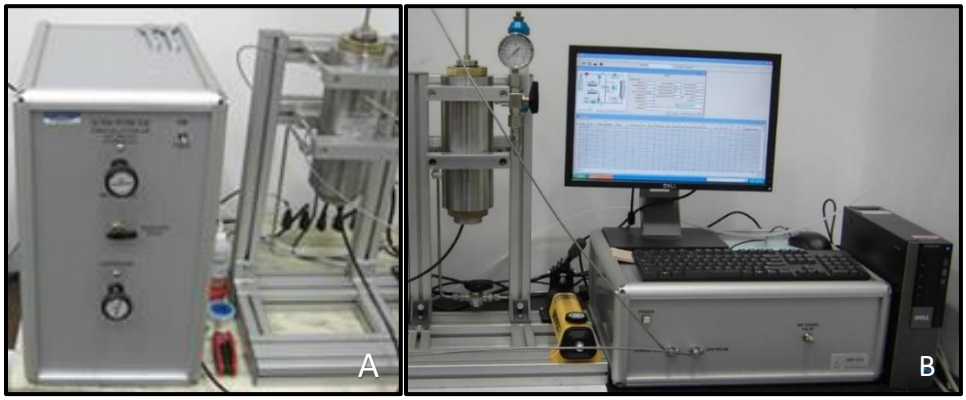

Figure 15: A) Flow through and B) pulse decay permeameters.

The New England Research company's AutoLab 1500 (Figure 16) was used to determine the mechanical properties of the samples. The test apparatus allows the user to vary confining pressures to simulate in-situ stresses as well as pressure changes induced during production or sequestration scenarios. The device generates and measures the P (compression) wave and two S- (S_1 and S_2) (shear) waves (perpendicular to one another) through the core. Dynamic elastic parameters (e.g., Young's Modulus and Poisson's Ratio) were derived using the obtained acoustic velocities.

Figure 16: NER AutoLab 1500 (left) and example sample array (right).

2.6 DATA COMPILATION

Strater® by Golden Software® was used to compile the MSCL and medical CT data into a series of geophysical logs. The data used to generate these logs can be accessed from NETL's Energy Data eXchange (EDX) online system using the following link: https://edx.netl.doe.gov/dataset/IMSCS-HUB_SHRU_86A_Core.

3. RESULTS

Processed 2D slices of the medical CT scans through the cores are shown first, followed by the XRF and magnetic susceptibility measurements of the core from the MSCL.

3.1 MEDICAL CT SCANS

The core from the IMSCS-HUB SHRU 86A well was scanned with a Toshiba Aquilion TSX-101A/R medical CT scanner at a sub-millimeter core-scale resolution (430 µm x 430 µm x 500 µm). The variation in greyscale values observed in the medical CT images indicates changes in the CTN obtained. That number, in turn, is directly proportional to changes in the attenuation and density of the scanned rock. Thus, darker regions in the scan are less dense than lighter-toned regions. The core was scanned in 3 ft or smaller sections obtained from each core box. In the following images, the overall depth for each scanned sub-section of core is listed. Many interesting features can readily be seen, including pyrite nodules, defined fracture planes, and very thin laminations.

3.1.1 XZ Planes

A 2D reslice image through the center of each retrieved core barrel is processed from the medical CT volumes (Figure 17). The images can be found in Figure 18 through Figure 25. These are referred to as "XZ" planes with the coordinates that are shown in Figure 17. The red scale bar shown in these images is 2 cm; the retrieved core has a diameter of 4 in. for reference. Black circular holes on reslice images are where a core plug was removed prior to scanning. The labels below each 2D XZ plane in Figure 18 through Figure 25 are the depth of each core and the full range of core lengths shown in each figure is listed in the figure captions. The greyscale values were individually shifted in these images to best represent the structures within each piece of core.

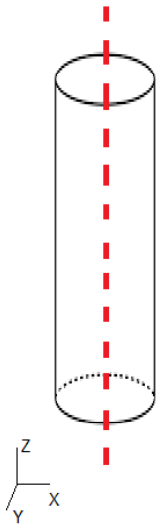

Figure 17: Schematic of the XZ isolated plane through the vertical center of the medical CT scans.

3.2 IMSCS-HUB SHRU 86A MEDICAL CT SCANS

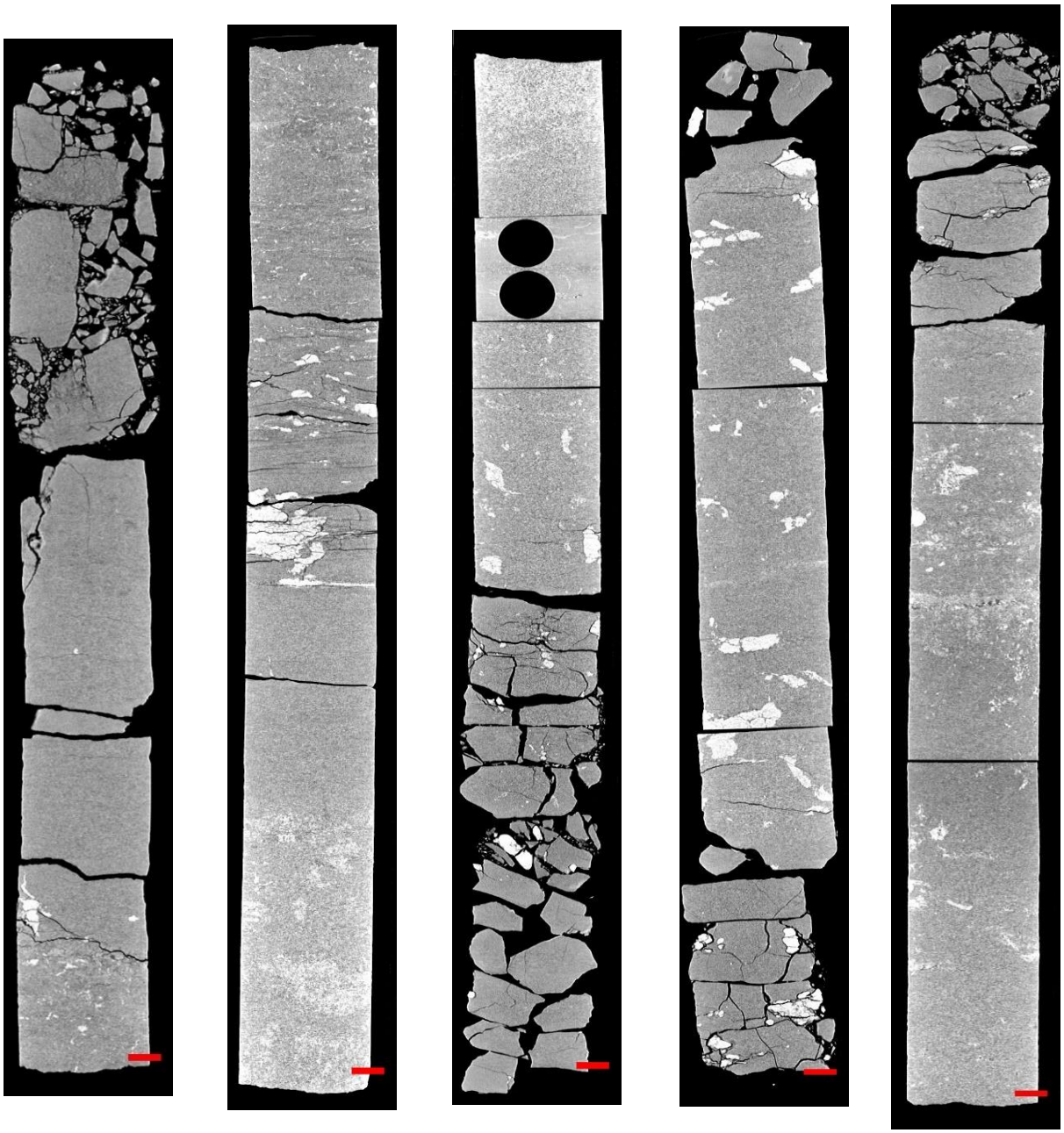

2,900-2,903 ft **2,903-2,906 ft** **2,906-2,909 ft** **2,909-2,912 ft** **2,912-2,915 ft**

Figure 18: 2D isolated planes through the vertical center of the medical CT scans of the IMSCS-HUB SHRU 86A well Core 1 from 2,900 to 2,915 ft.

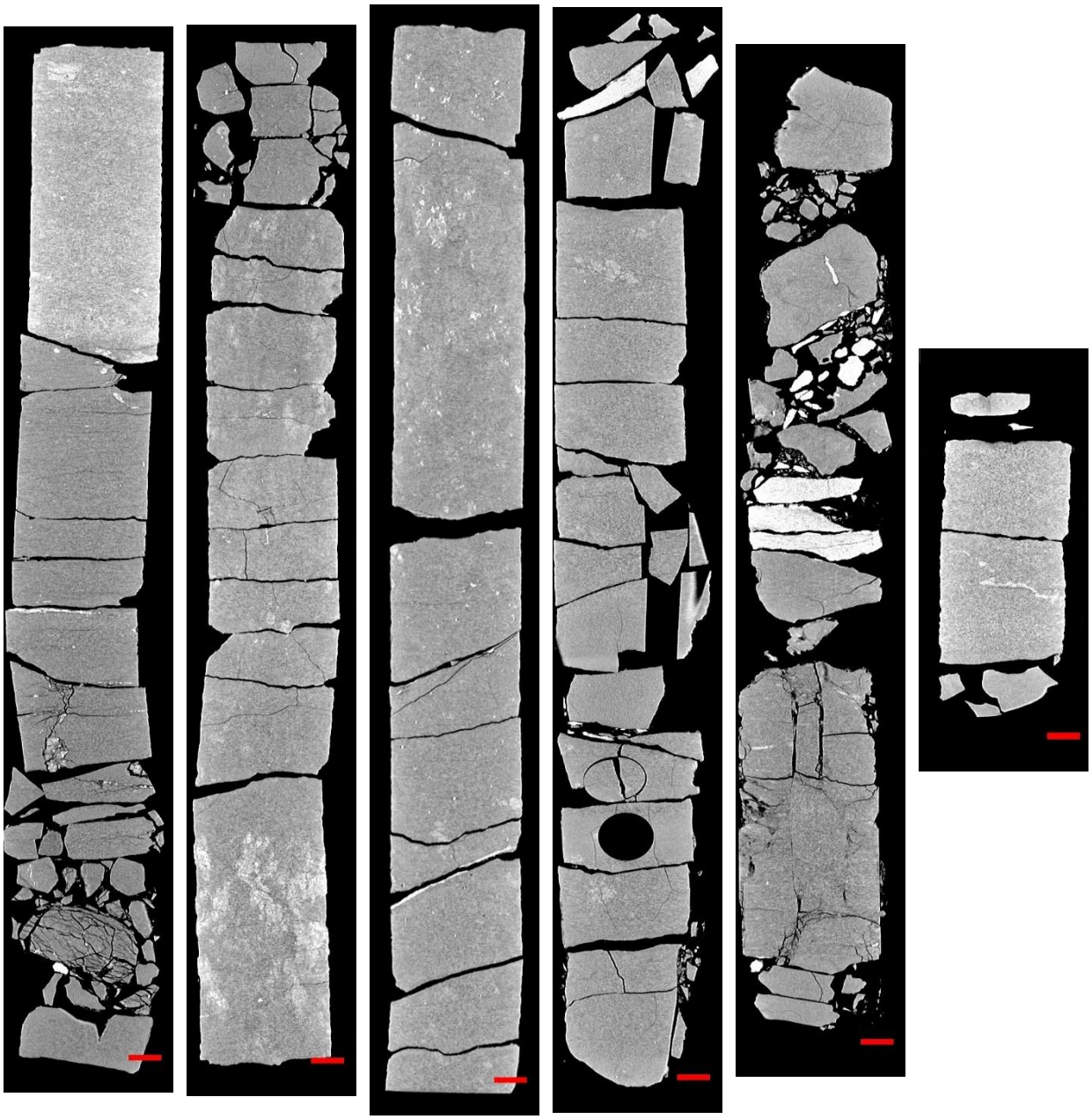

2,915-2,918 ft **2,918-2,921 ft** **2,921-2,924 ft** **2,924-2,927 ft** **2,927-2,930 ft** **2,930-2,931 ft**

Figure 19: 2D isolated planes through the vertical center of the medical CT scans of the IMSCS-HUB SHRU 86A well Core 1 from 2,915 to 2,931 ft.

3,009-3,012 ft **3,012-3,015 ft** **3,015-3,018 ft** **3,018-3,021 ft** **3,021-3,024 ft**

Figure 20: 2D isolated planes through the vertical center of the medical CT scans of the IMSCS-HUB SHRU 86A well Core 2 from 3,009 to 3,024 ft.

3,024-3,027 ft **3,027-3,030 ft** **3,030-3,033 ft** **3,033-3,036 ft** **3,036-3,039 ft**

Figure 21: 2D isolated planes through the vertical center of the medical CT scans of the IMSCS-HUB SHRU 86A well Core 2 from 3,024 to 3,039 ft.

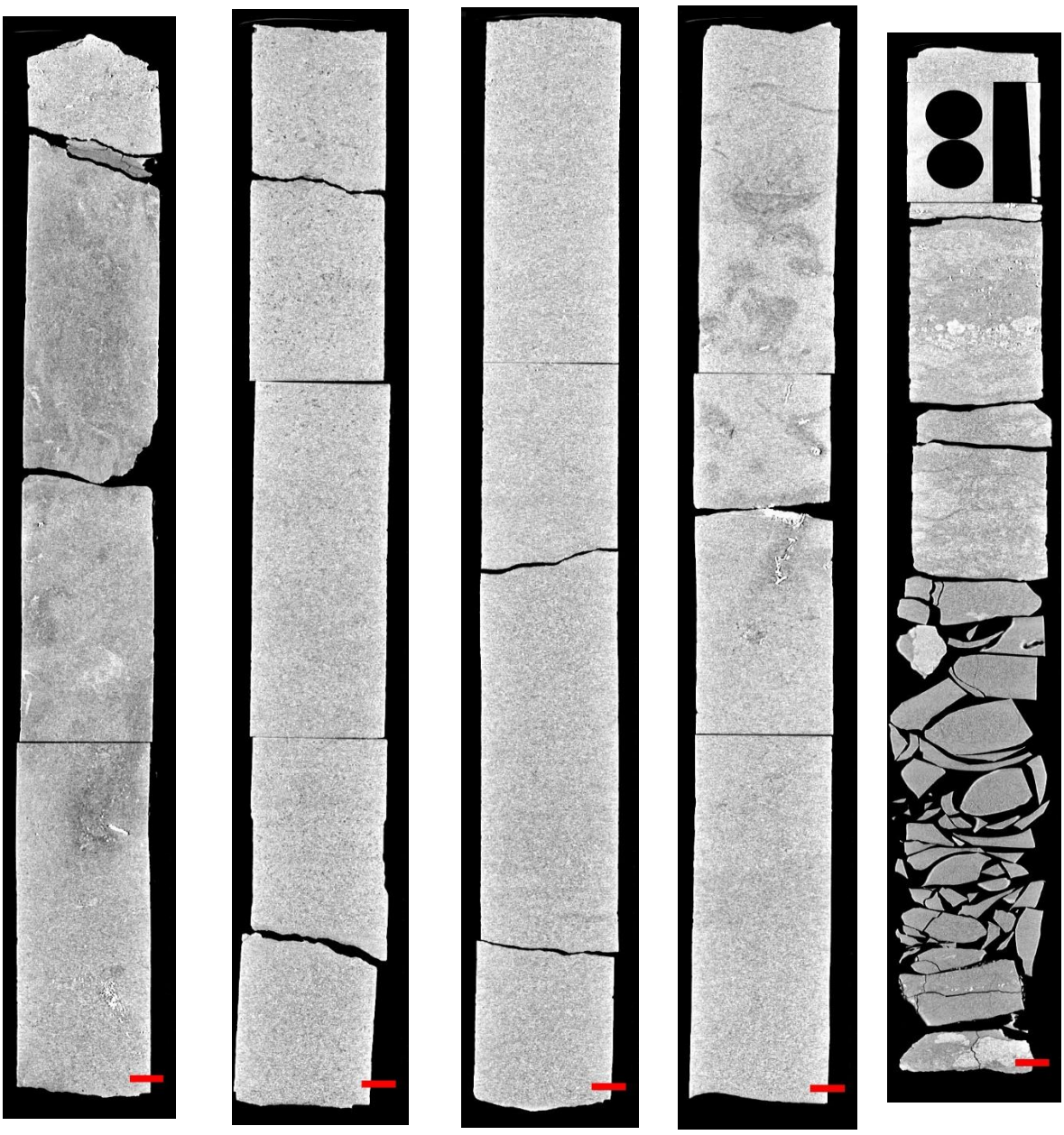

3,161-3,164 ft **3,164-3,167 ft** **3,167-3,170 ft** **3,170-3,173 ft** **3,173-3,176 ft**

Figure 22: 2D isolated planes through the vertical center of the medical CT scans of the IMSCS-HUB SHRU 86A well Core 3 from 3,161 to 3,176 ft.

3,176-3,179 ft **3,179-3,182 ft** **3,182-3,185 ft** **3,185-3,188 ft** **3,188-3,191 ft**

Figure 23: 2D isolated planes through the vertical center of the medical CT scans of the IMSCS-HUB SHRU 86A well Core 3 from 3,176 to 3,191 ft.

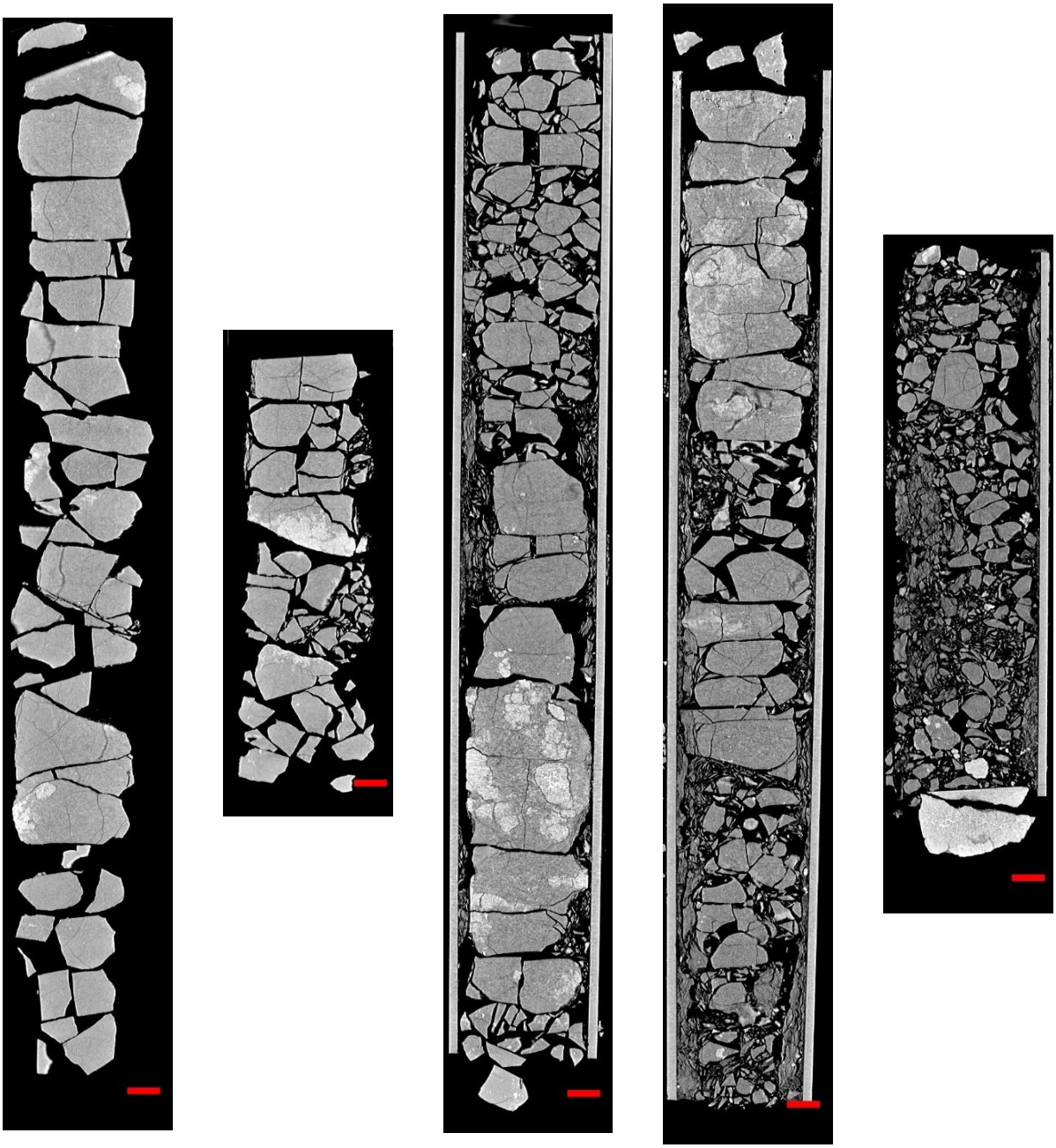

3,479-3,482 ft **3,482-3,483 ft** **3,483-3,486 ft** **3,486-3,489 ft** **3,489-3,491 ft**

Figure 24: 2D isolated planes through the vertical center of the medical CT scans of the IMSCS-HUB SHRU 86A well Core 4 from 3,479 to 3,491 ft.

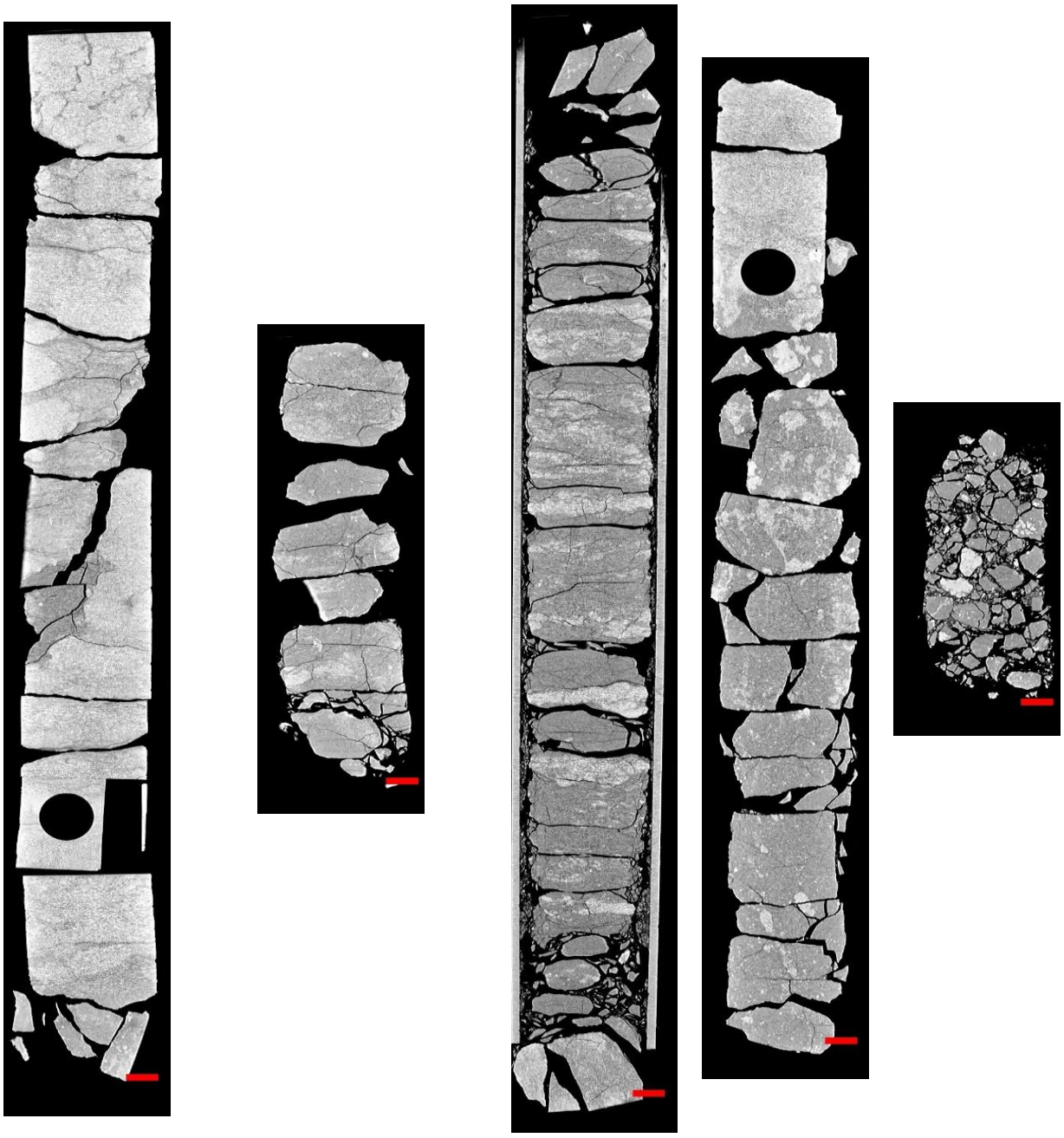

3,491-3,494 ft **3,494-3,495 ft** **3,495-3,498 ft** **3,498-3,501 ft** **3,501-3,502 ft**

Figure 25: 2D isolated planes through the vertical center of the medical CT scans of the IMSCS-HUB SHRU 86A well Core 4 from 3,491 to 3,502 ft.

3.3 ADDITIONAL CT DATA

Additional CT data can be accessed from NETL's EDX online system using the following link: https://edx.netl.doe.gov/dataset/IMSCS-HUB_SHRU_86A_Core. The original CT data is available as 16-bit tif stacks suitable for reading with ImageJ (Schneider et al., 2012) or other image analysis software.

3.3.1 Medical CT Image Videos

In addition, videos showing the variation along the length of the cross-section images shown in the previous section are available for download and viewing. At depths from 3,033 to 3,036 ft, where darker regions represent mudrock and lighter areas represent a wackestone, fossilized remains of crinoids and shell fragments are visible (Figure 26). Here, the red line through the XZ-plane image of the core shows the location of the XY-plane image displayed in the core at the top of the image. The videos on EDX show this XY variation along the entire length of the core.

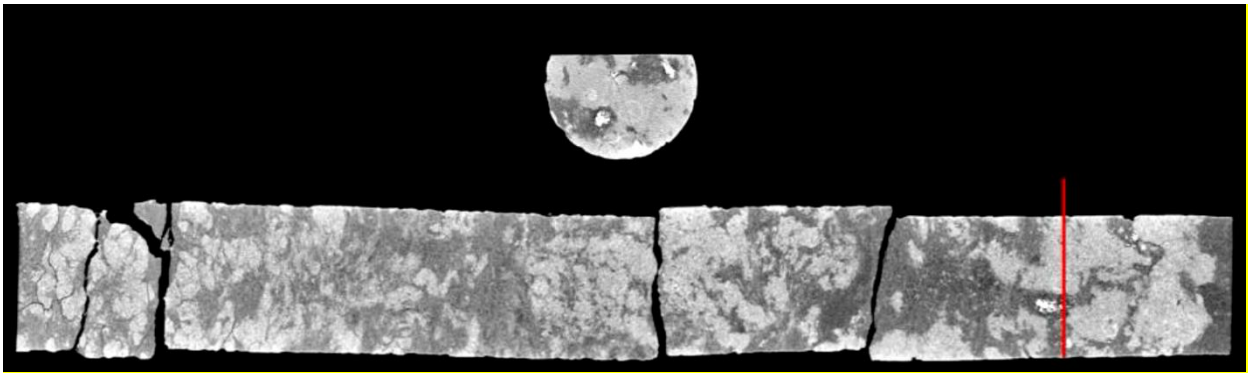

Figure 26: Single image from a video file available on EDX showing variation in the IMSCS-HUB SHRU 86A core from 3,033 to 3,036 ft. Image at the top shows the variation in composition within the matrix perpendicular to the core length. Note the bright (high density) nodules in the matrix.

3.3.2 Industrial CT Scanning

Detailed scans of sections of interest were performed by the NorthStar Imaging Inc. M-5000® Industrial Computed Tomography System (Industrial CT) at NETL. The system was used to obtain higher resolution scans with voxel resolution between 20.1 and 100.4 μm^3 (Table 2) and capture the details of certain features clearly. The whole core scans were performed at a voltage of 185 kV and a current of 400 µA and scans of core plugs were performed at 185kV and 200 µA. These settings provided the appropriate photon energy to penetrate the samples. The samples were rotated 360° and 1,440 radiograph projections of the samples were obtained, averaging 12 individual radiographs at each step to create the reconstruction. Resampled images illustrating the variation along the length of each volume are shown in Figures 27 through 29.

Table 2: Industrial Scans from Plugs and Whole Core, All Available on EDX

Depth (ft)	File Name	Resolution (μm^3)
2,903	RedWill_C-1_Bx-1_2903_MIC	71.1
2,903	RedWillow_2903-2906	20.1
2,906	RedWillow_2906-2909	20.1
3,022.4	RedWill_C-2_Bx-7_3022-4_MIC	62.1
3,024	RedWillow_3024-3027	20.1
3,027.8	RedWill_C-2_Bx-7_3027-8_MIC	62.1
3,033.8	RedWill_C-2_Bx-9_3033-8_MIC	71.1
3,034	RedWill_C-2_Bx-9_3034_MIC	71.1
3,101.3	RedWill_C-2_Bx-7_3027-8_MIC	67.2
3,188	RedWillow_3188-3191	20.1
3,491	RedWillow_3491-3494	20.1
3,499	RedWill_C-4_Bx-9_3499_MIC	71.1

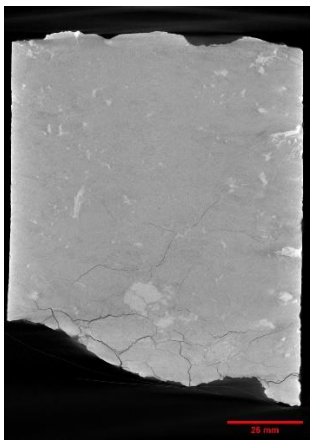

2,903 ft

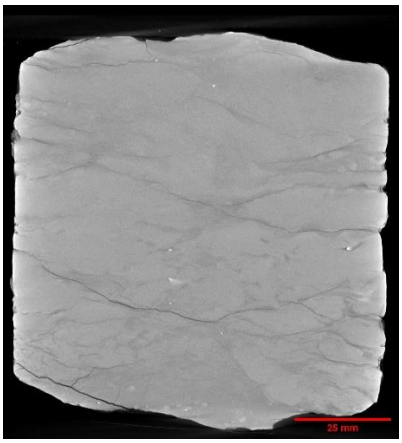

3,022 ft

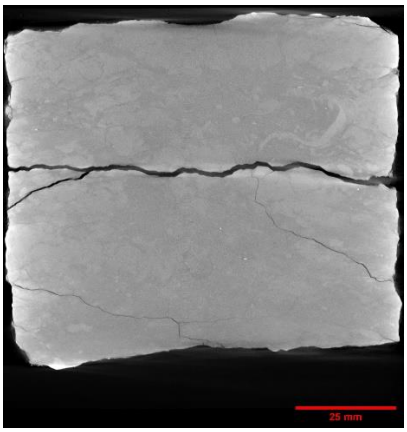

3,027.8 ft

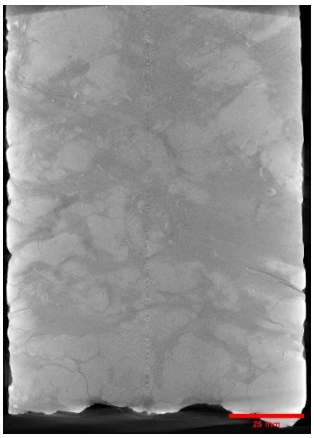

3,033.8 ft

Figure 27: **2D isolated planes through the vertical center of the Industrial CT scans of the IMSCS-HUB SHRU 86A well from 2,903 ft to 3,033.8 ft.**

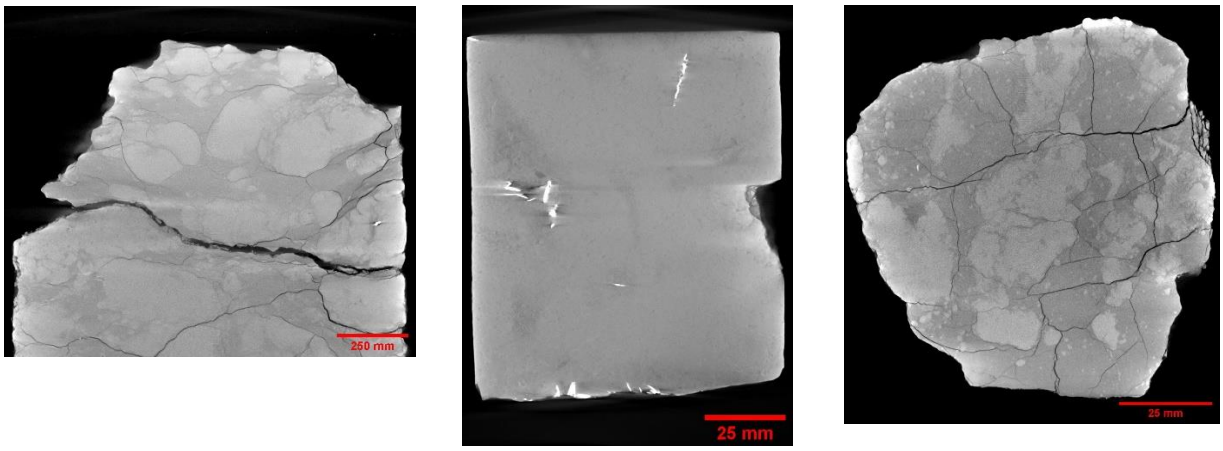

3,073.4 ft **3,101.3 ft** **3,499 ft**

Figure 28: 2D isolated planes through the vertical center of the Industrial CT scans of the IMSCS-HUB SHRU 86A well from 3,073.4 ft to 3,499 ft.

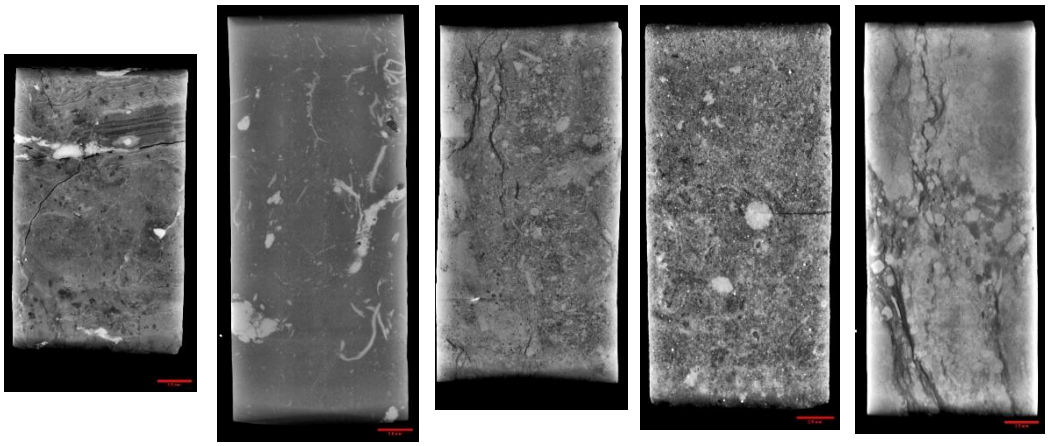

2,903 ft **2,906 ft** **3,024 ft** **3,188 ft** **3,491 ft**

Figure 29: 2D isolated planes through the vertical center of the Industrial CT scans of the 1-in. diameter subcores from the IMSCS-HUB SHRU 86A well measured with the AutoLab 1500 and PDP.

3.3.3 Micro CT Scans

Detailed micro-CT scans of mm-scale core plugs from select regions were performed at NETL using the EISS Xradia micro-CT scanner (discussed in Section 2.4) to obtain higher resolution images with a voxel resolution of 2.15 μm^3 and capture the details of internal features. A list of the core sections scanned with the micro-CT scanner is shown in Table 3, followed by images from these scanned volumes along the XY and XZ planes of these small cores. Resampled images representing each volume are shown in Figure 30 and Figure 31.

Table 3: Micro-CT Scans from Whole Core

Depth	File Name	Resolution (μm^3)
2,924.75	20210409 Red Willow 2924.75	2.15
3,036.0	20210406 Red Willow 3036	2.15

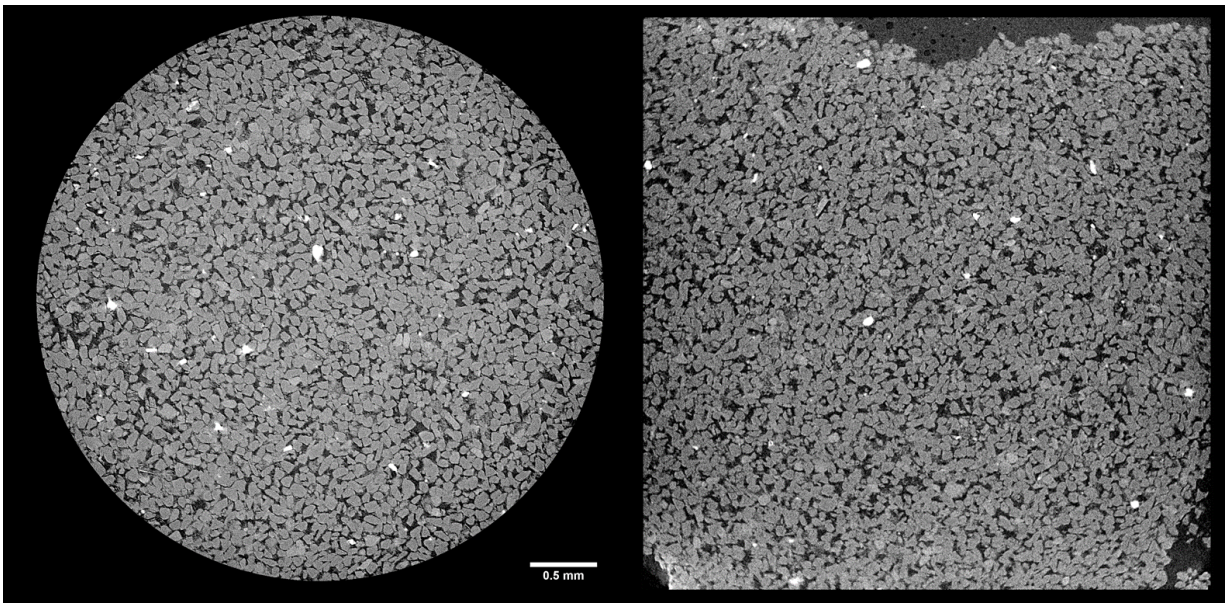

Figure 30: Horizontal (left) and vertical (right) slices of micro-CT scans of 20210409 Red Willow 2,924.75 ft.

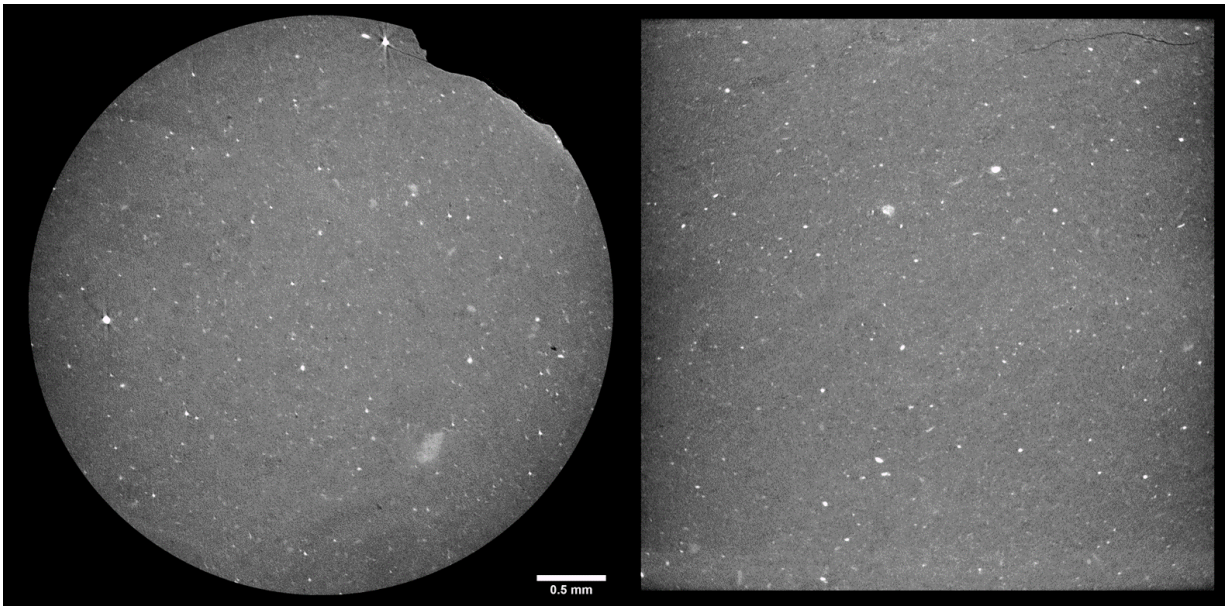

Figure 31: Horizontal (left) and vertical (right) slices of micro-CT scans of 20210406 Red Willow 3,036 ft.

3.4 DUAL ENERGY CT SCANNING

Dual energy CT scanning uses two sets of images, produced at different X-ray energies, to approximate the density (ρ_B) (Siddiqui and Khamees, 2004; Johnson, 2012). The technique relies on the use of several standards of known ρ_B to be scanned at the same energies as the specimen. These scans are performed at lower energies (<100 KeV) and higher energies (>100 KeV) to induce two types of photon interactions with the object (Figure 32). The lower energy scans induce photoelectric absorption, which occurs when the energy of the photon is completely absorbed by the object mass and causes ejection of an outer orbital electron (Figure 32a). The high energy scans induce Compton scattering, which causes a secondary emission of a lower energy photon due to incomplete absorption of the photon energy in addition to an electron ejection (Figure 32b).

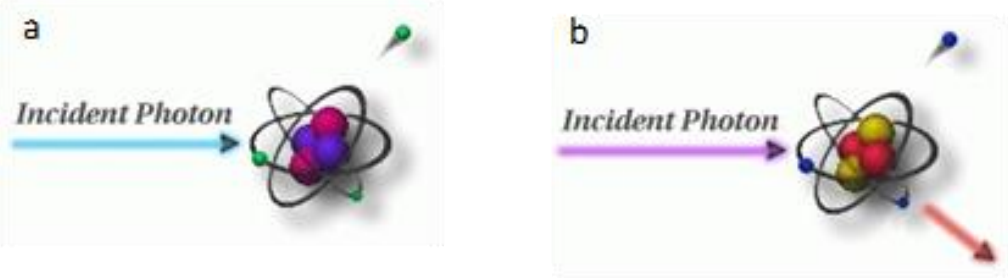

Figure 32: Photon interactions at varying energies, (A) photoelectric absorption and (B) Compton scattering. Iowa State University Center for Nondestructive Evaluation (2021).

Medical grade CT scanners are typically calibrated to known standards, with the output being translated in CTN or Hounsfield Units (HU). Convention for HU defines air as -1,000 and water as 0. A linear transform of recorded HU values is performed to convert them into CTN. This study used CTN as it is the native export format for the instrument, but it is possible to use HU. Dual energy CT requires at least three calibration points, and it is prudent to utilize standards that approximate the object or material of interest. Pure samples of aluminum, graphite, and sodium chloride were used as the calibration standards as they most closely approximate the rocks and minerals of interest (Table 4). Most materials denser than water or with higher atomic masses have a non-linear response to differing CT energies (Table 5).

Table 4: Dual Energy Calibration Standards, Bulk Density (g/cm^3)

Material	ρ_B (g/cm^3)
Air	-0.001
Water	1
Graphite	2.3
Sodium Chloride	2.16
Aluminum	2.7

Table 5: Dual Energy Calibration Standards, HU and CTN for "Low" and "High" Energies

Material	HU		CTN	
	80 KeV	135 KeV	80 KeV	135 KeV
Air	-993	-994	31,775	31,774
Water	-3.56	-2.09	32,764	32,766
Graphite	381	437	33,149	33,205
Sodium Chloride	1,846	1,237	34,614	34,005
Aluminum	2,683	2,025	35,451	34,793

Dual energy CT utilizes these differences to calibrate to the X-ray spectra. Two equations with three unknowns each are utilized to find ρ_B (Siddiqui and Khamees, 2004):

$$\rho_B = mCTN_{low} + pCTN_{high} + q$$

Where [m, p, and q] are unknown coefficients that can be solved by setting up a system of equations with four 3 x 3 determinants. The CTN is obtained from the CT scans for each of the homogenous calibration standards.

In this study, the high and low energy image stacks were loaded into Python as arrays. A 3D Gaussian blur filter with a sigma of 2 was used to reduce noise in the images. The scipy.solv module of Python was then employed to solve for the coefficients based on the calibration standard CTN values. The ρ_B was solved for each pixel in the 3D volume and saved as two new separate image stacks.

3.5 COMPILED CORE LOG

The compiled core logs were scaled to fit on single pages for rapid review of the combined data from the medical CT scans and MSCL readings. Nine core logs were made to represent the core logger data: Figure 33, represents all cored sections and the associated porosity and permeability data in Section 1.8; and Figure 34 through Figure 41, are represented by two sets of logs presented for each cored section (Core 1 from 2,900 to 2,930 ft; Core 2 from 3,009 to 3,038.5 ft; Core 3 from 3,161 to 3,190.8 ft; and Core 4 from 3,479 to 3,500 ft). The first set has data from the major elements and elemental ratios, and the second set has data from elemental proxies and CT image data (dual energy density). Features that can be derived from these combined analyses include determination of mineral locations, such as pyrite, from magnetic susceptibility. The XRF can be used to inform geochemical composition and mineral form.

Data from the MSCL was filtered to remove areas of fractures and missing core. P-wave velocity was limited to values greater than 330 m/s and gamma density (and dual energy density) were limited to values greater than 1.5 g/cm^3.

The elemental results from the XRF were limited to major elements (LE, Ca, Si, Al) and elemental proxies related to redox potential (Ni and V), biogenic production (P and V*), skeletal influx/carbonate potential (Ca and Mn), detrital influence (Zr, Ti, Al, Si), and chalcophiles (Pb, S, Fe).

Trends in elemental ratios can provide insight into variations in mineral composition, oxidation state, and depositional setting. A short description of how these are representative of various geological processes is listed in Table 6.

The elemental proxy log also includes an XRF “mineralogy” with Al (grey), representing clays; Ca (blue), representing calcite; and Si (yellow), representing quartz, although there is some Si contribution from the clays. Pyrite (reduced) should have low magnetic susceptibility, and Fe oxide or hydroxide should have high magnetic susceptibility. These broad trends can quickly give information over large lengths of core and direct more focused research to zones of potential interest. These logs are presented Figure 34 through Figure 41.

Table 6: Elemental Ratios and Their Significance

Elemental Ratio	Marker for:	Lower Value	Higher Value
Si/Al	Abundance of illite and micas vs. other clays	More of other clay types (e.g., kaolinite-group and smectite-group minerals)	More illite and micas
Ti/Al	Input of terrigenous sediment	Less input of sediment eroded from land	More input of sediment eroded from land
Ca/Mg	Dolomite	More dolomitic	Less dolomitic
Ca/Si	Relative abundance of calcium carbonates vs. silicates	Silicate-mineral-rich sediments	Carbonate-rich sediments
S/Fe	Abundance of pyrite (and other iron sulfates) vs. other Fe oxide metals	Fe-oxide dominate/sulfate lean	Sulfate rich
Fe/Al	Degree of pyritization in shales	Lower degree of pyritization	Higher degree of pyritization
Mn/Fe	Oxidation	More anoxic/euxinic	More dysoxic/oxic

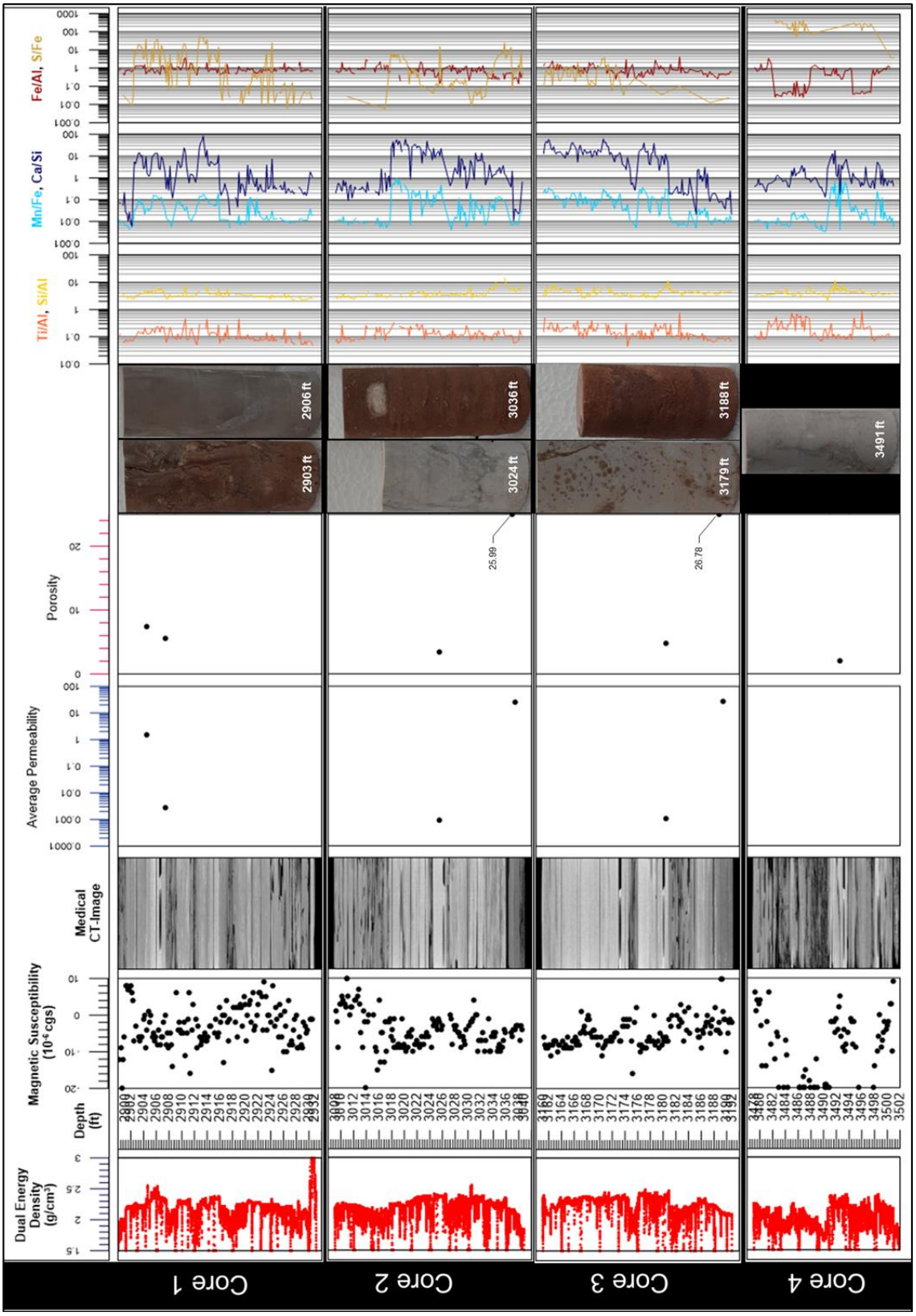

Figure 33**: Compiled core log for IMSCS-HUB SHRU 86A well AutoLab 1500 measured porosity and permeability.**

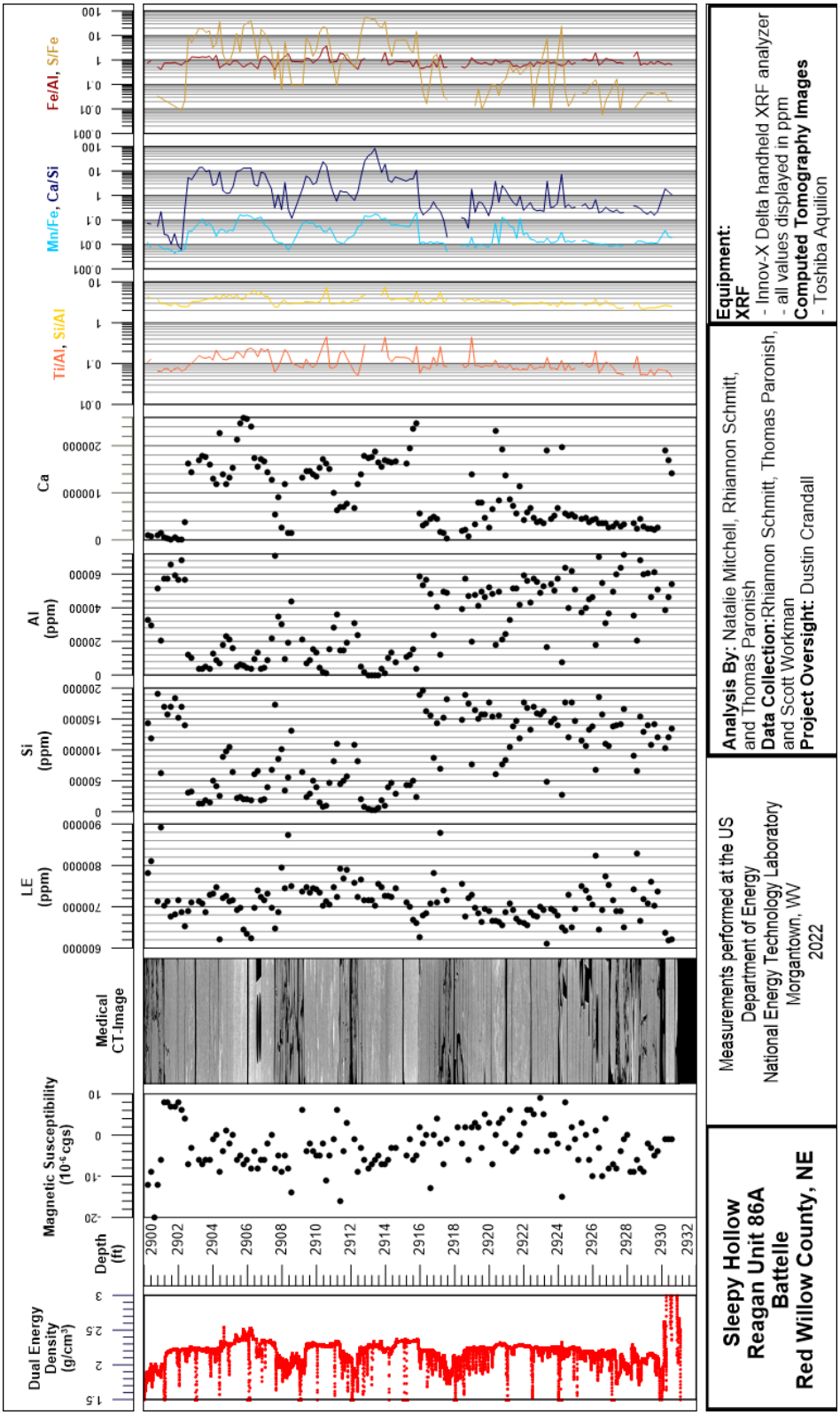

Figure 34: Compiled core log for IMSCS-HUB SHRU 86A Core 1, with major elements and elemental ratios, from 2,900 to 2,930 ft.

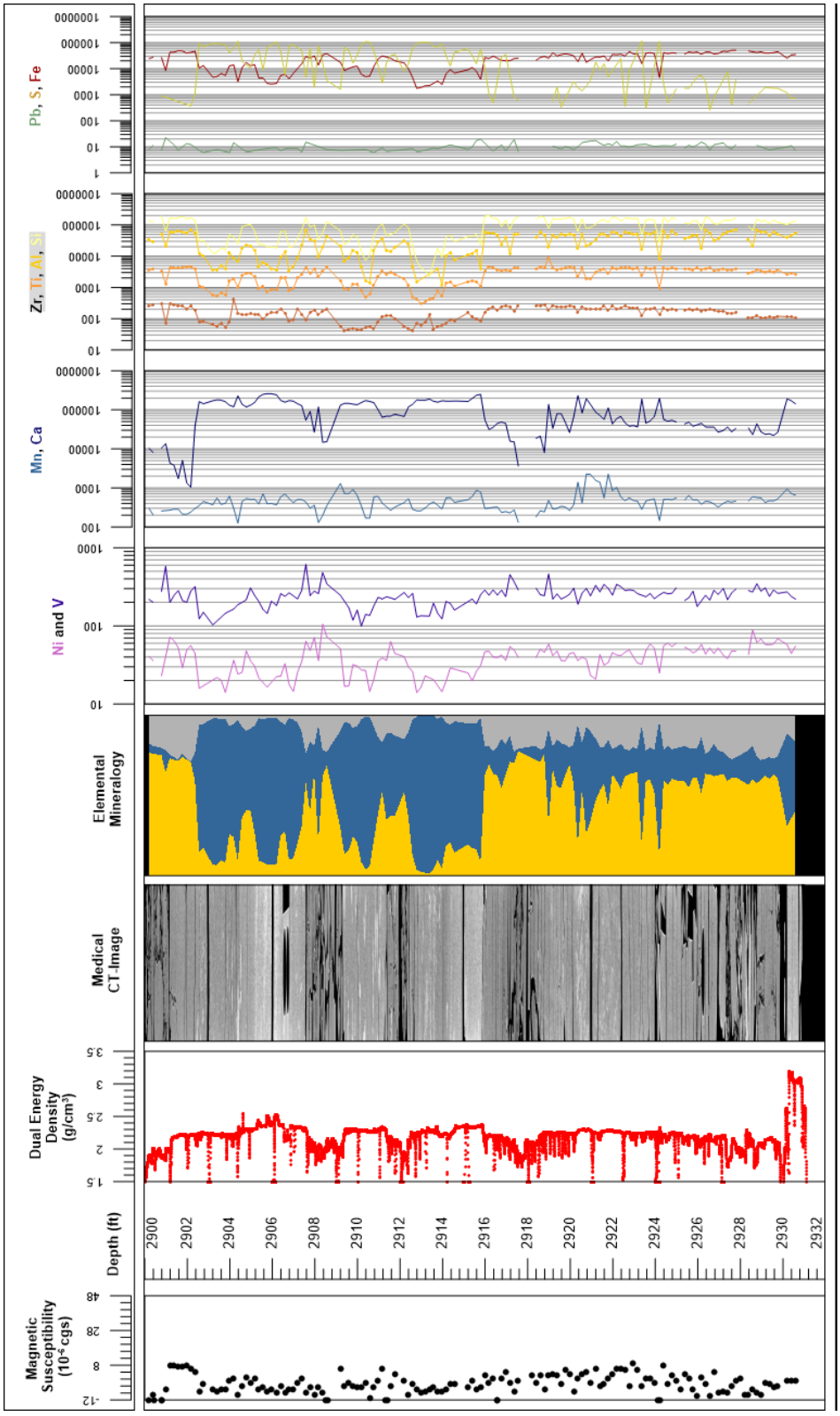

Figure 35: Compiled core log with elemental proxies for IMSCS-HUB SHRU 86A Core 1, from 2,900 to 2,930 ft.

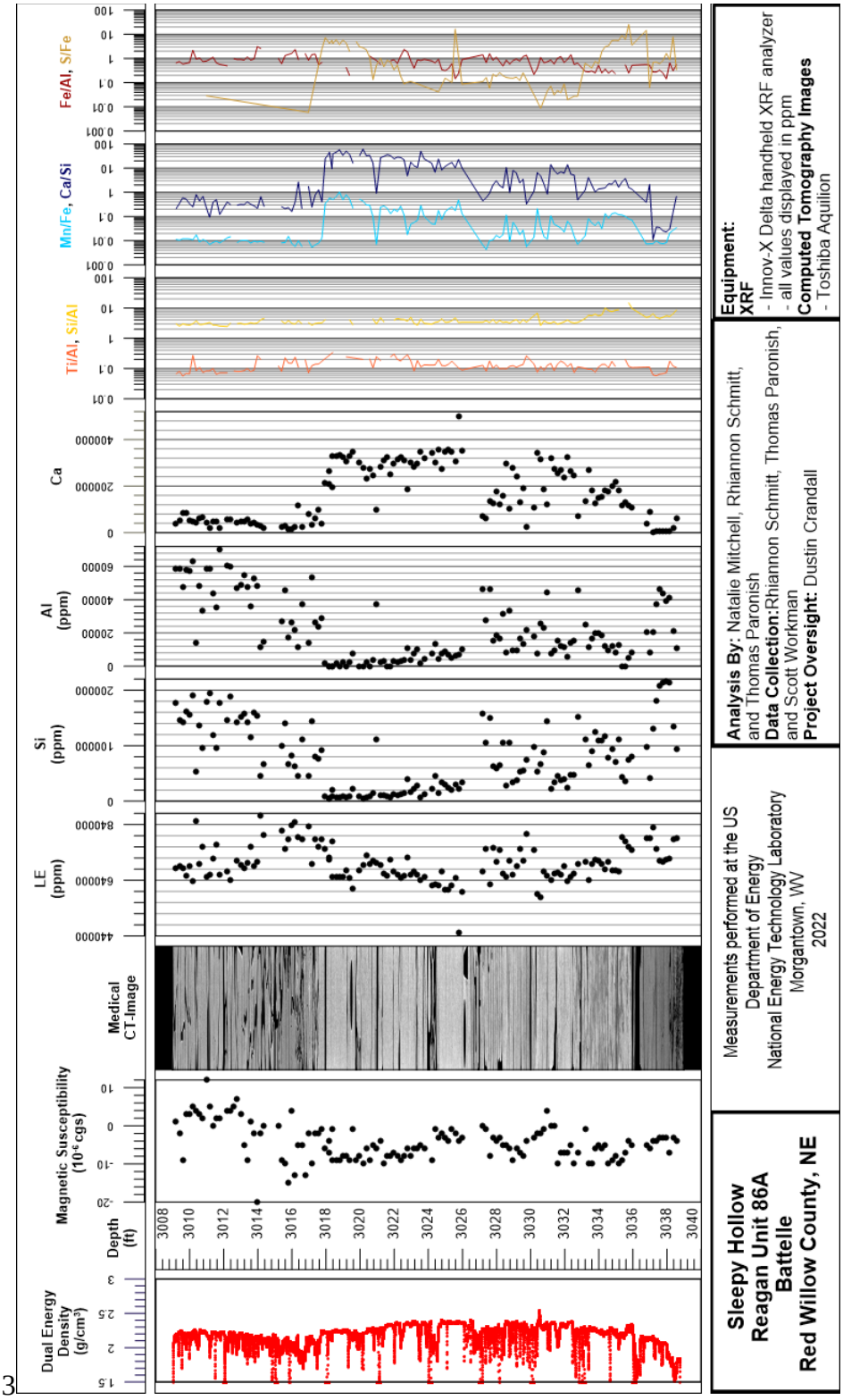

Figure 36: Compiled core log for IMSCS-HUB SHRU 86A Core 2, with major elements and elemental ratios, from 3,009 to 3,038.5 ft.

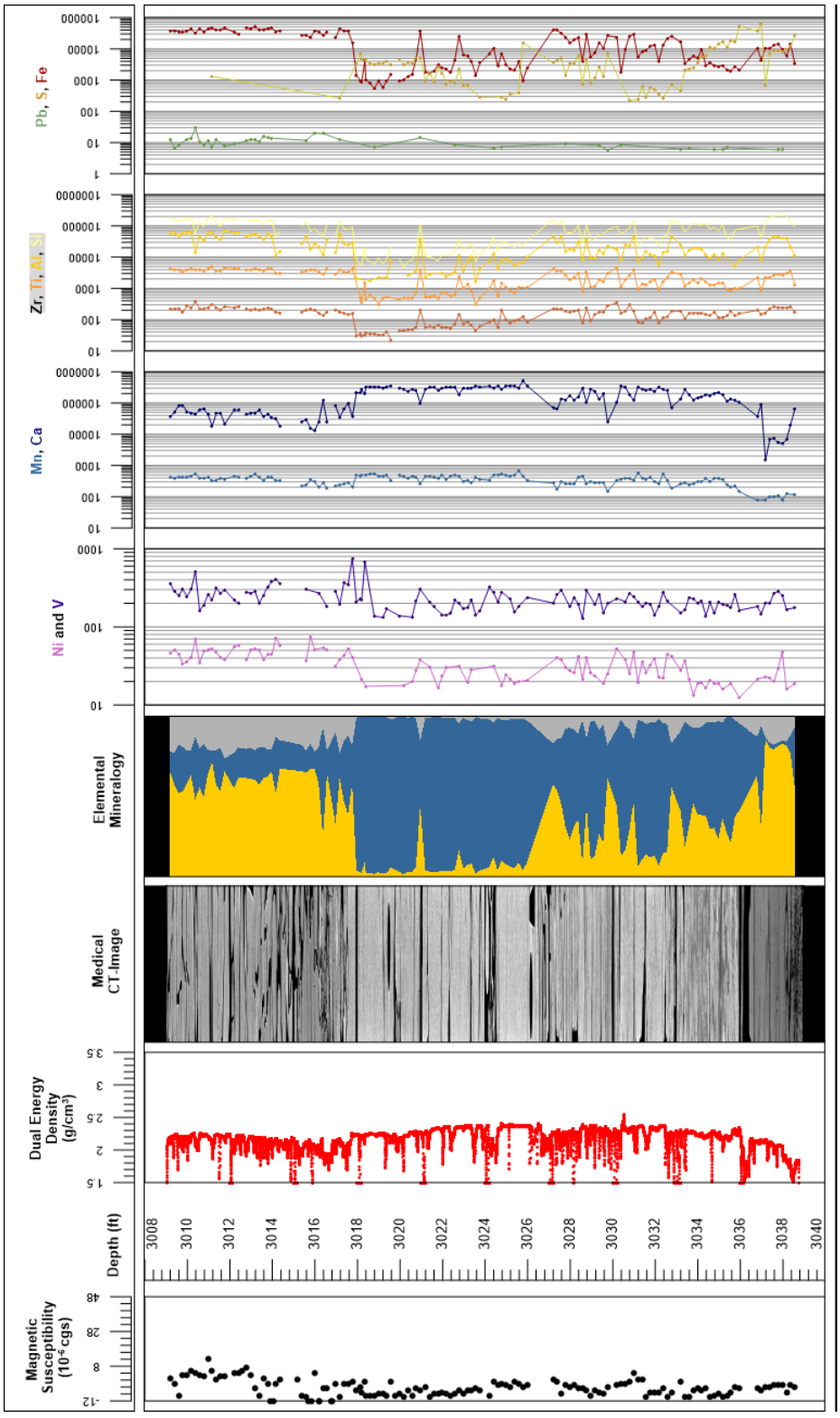

Figure 37: Compiled core log with elemental proxies for IMSCS-HUB SHRU 86A Core 2, from 3,009 to 3,038.5 ft.

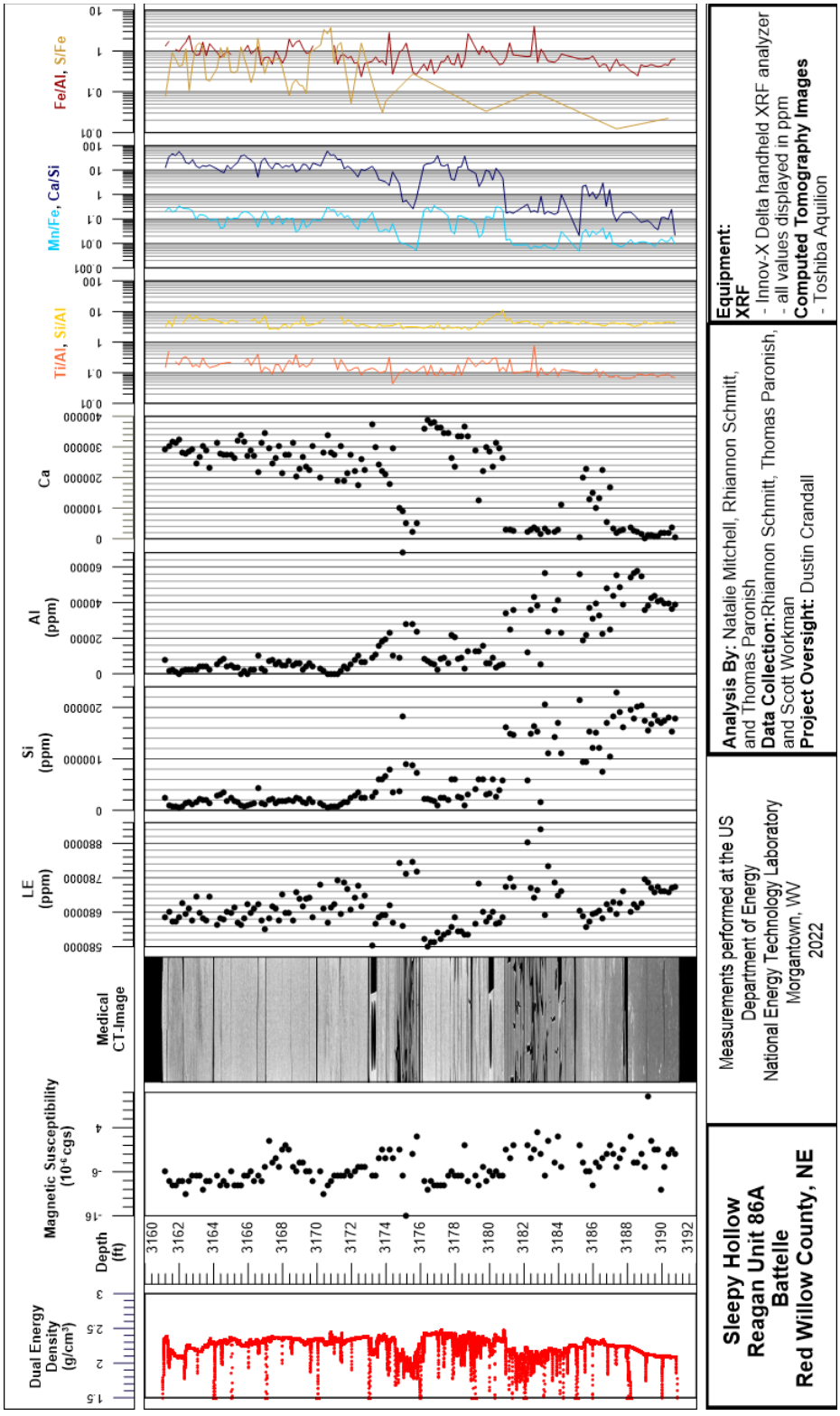

Figure 38: Compiled core log for IMSCS-HUB SHRU 86A Core 3, with major elements and elemental ratios, from 3,161 to 3,190.8 ft.

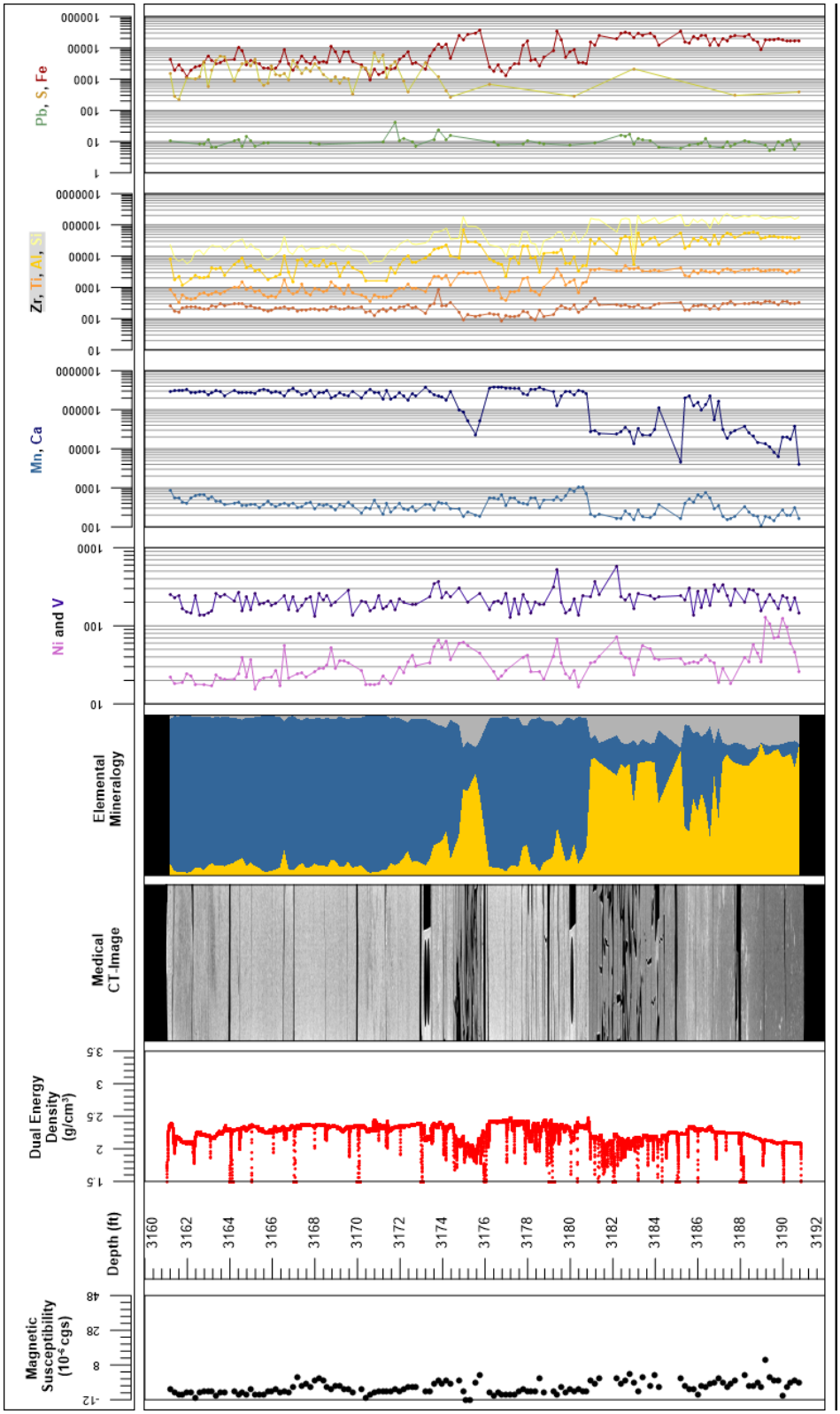

Figure 39: Compiled core log with elemental proxies for IMSCS-HUB SHRU 86A Core 3, from 3,161 to 3,190.8 ft.

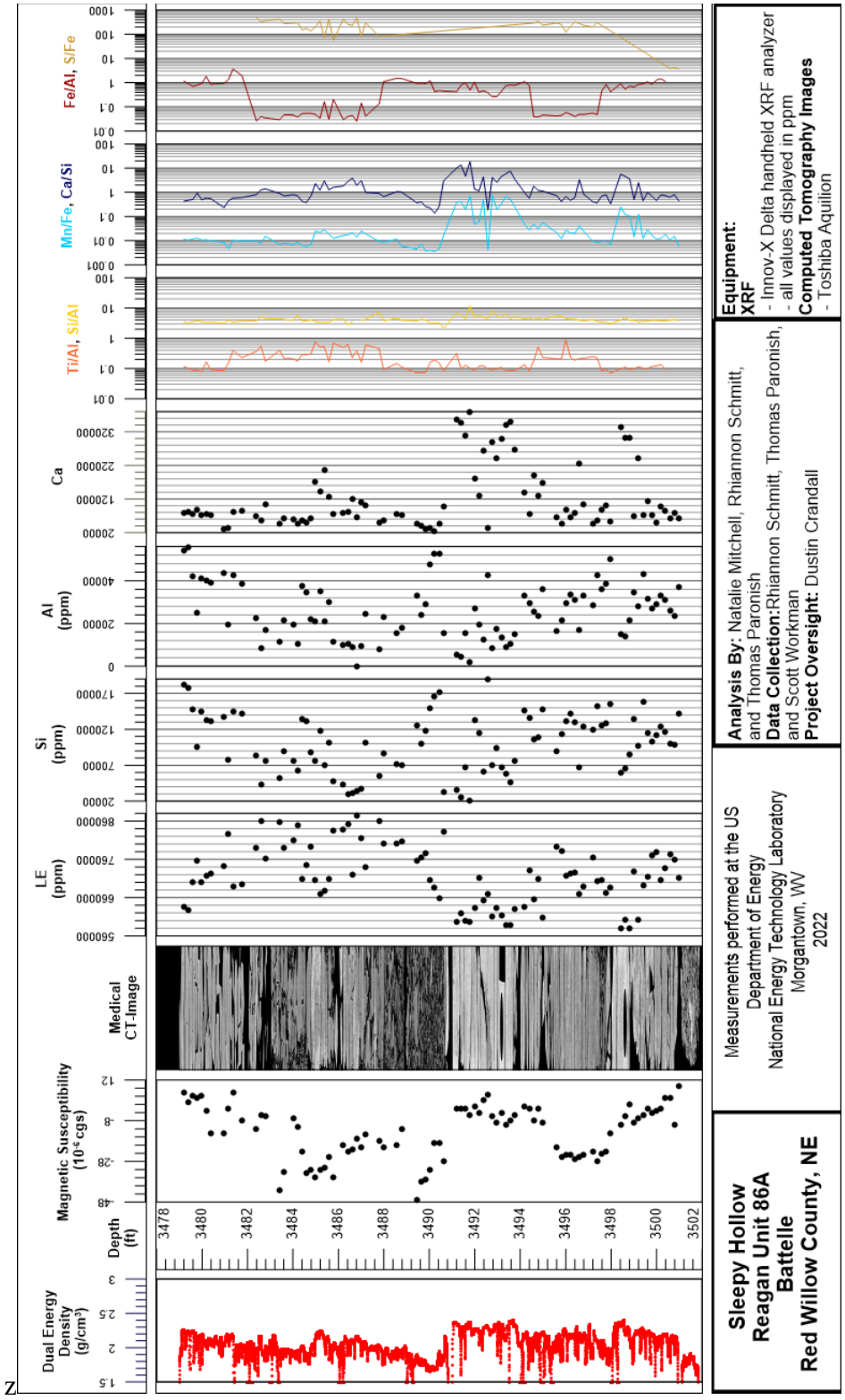

Figure 40: Compiled core log for IMSCS-HUB SHRU 86A Core 4, with major elements and elemental ratios, from 3,479 to 3,500 ft.

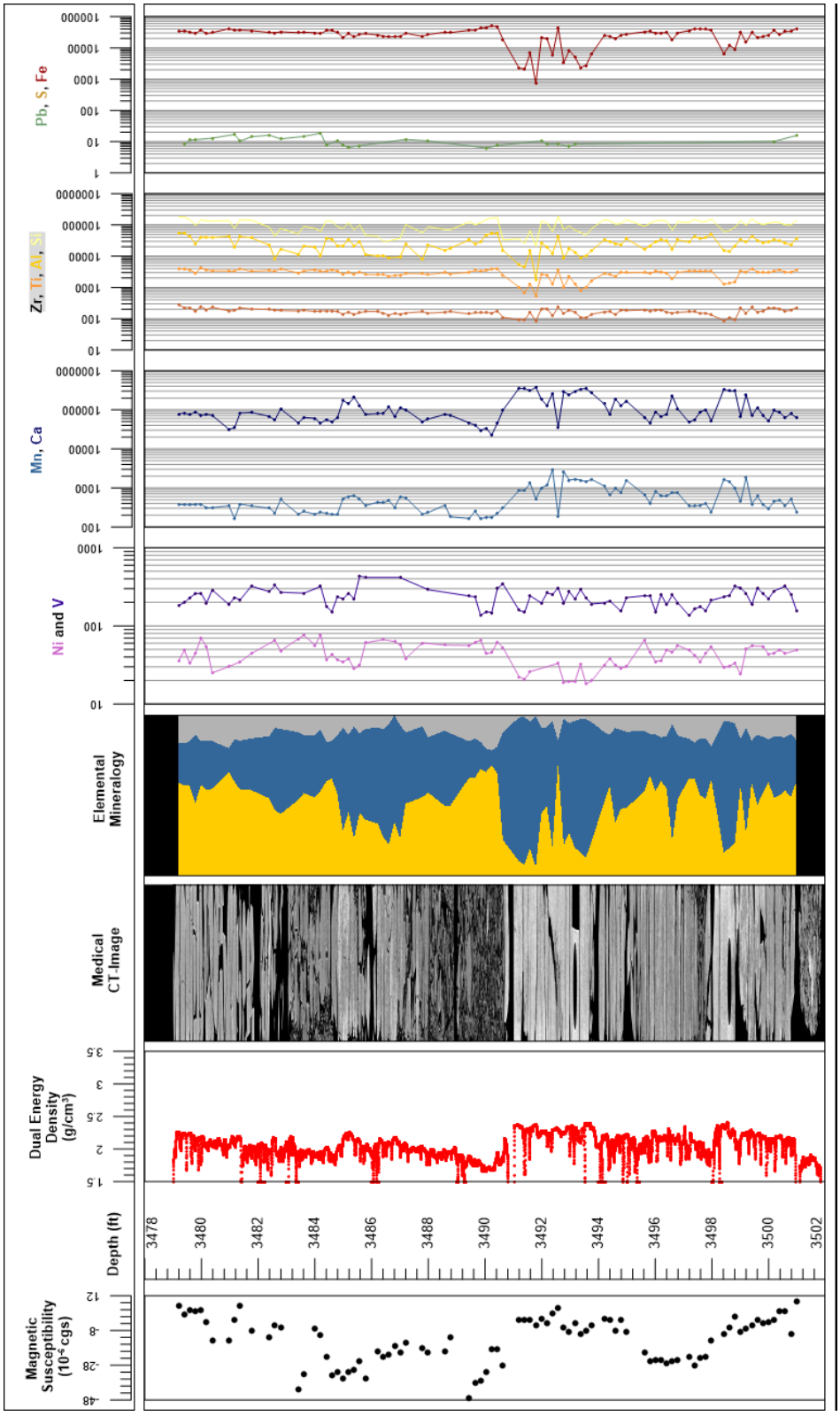

Figure 41: Compiled core log with elemental proxies for IMSCS-HUB SHRU 86A Core 4, from 3,479 to 3,500 ft.

3.6 PERMEABILTY, POROSITY, AND GEOMECHANICS

Little directional dependence was observed when comparing the two shear wave velocities (Figure 42). All supplemental experimental data for porosity, permeability, and geomechanical measurements are available on NETL's EDX: https://edx.netl.doe.gov/dataset/IMSCS-HUB_SHRU_86A_Core.

The laboratory equipment used for these measurements are located at NETL Pittsburgh and are described in Spaulding et al. (2024) (see also the "Geologic Storage Core Flow Laboratory" factsheet for more details).

Permeability data was acquired via the UltraPerm-500 for four samples at three different depths (2,903-2,906 ft cores differ in orientation of the bedding plane):

1. 2,903-2,906 ft (0.3 mD) parallel to bedding
2. 2,903-2,906 ft (0.06 mD) perpendicular to bedding
3. 3,036-3,039 ft (21 mD) parallel to bedding
4. 3,188-3,191 ft (22.7 mD) parallel to bedding

The PDP-200 was used to measure permeabilities for five samples from four different depths, as previously noted, this device was utilized due to the tight nature of these samples (3,179-3,182 ft cores differ in orientation of the bedding plane):

1. 2,906-2,909 ft (0.0029 mD) parallel to bedding
2. 3,024-3,027 ft (0.0009 mD) parallel to bedding
3. 3,179-3,182 ft (0.001 mD) parallel to bedding
4. 3,179-3,182 ft (0.0002 mD) perpendicular to bedding
5. 3,491-3,494 ft (0.0003 mD) parallel to bedding

The PDP-200 tests utilized a confining pressure of 2,000 psi and a test pressure of 750 psi, for a total effective pressure of 1,250 psi. The UltraPerm 500 used an effective pressure of 1,200 psi. Full results from these tests are available in Table 7 and Table 8.

Table 7: Summary of Permeability Result from the PDP-200 and UltraPerm-500

Depth (ft)	Orientation to Bedding	Formation/Group	Dry Bulk Density (g/cc)	Porosity (%)	UltraPerm-500 (mD)	PDP-200 (mD)
2,903	Parallel	Admire Group	2.23	7.46	0.3424	NA
2,903 (p)	Perpendicular	Admire Group	2.23	8.90	0.0620	NA
2,906	Parallel	Admire Group	2.55	5.63	NA	0.0029 ±0.0009
3,024	Parallel	Wabaunsee Group	2.57	3.40	NA	0.0009
3,036	Parallel	Wabaunsee Group	1.97	25.99	21.2600	NA
3,179	Parallel	Oread Fm./Lansing-Kansas City Group	2.54	4.86	NA	0.0010
3,179 (p)	Perpendicular	Oread Fm./Lansing-Kansas City Group	2.53	5.30	NA	0.0002
3,188	Parallel	Heebner Fm./Lansing-Kansas City Group	1.94	26.78	22.7100	NA
3,491	Parallel	lower Kansas City Fm./Lansing-Kansas City Group	2.63	2.08	NA	0.0003

Note: PDP-200 measurements were repeated, and the standard deviation is provided. Permeabilities obtained from PDP-200 were at 1,250 psi effective pressure and UltraPerm500 was collected at 1,200 psi.

Table 8: Geomechanical Results Obtained Using AutoLab 1500 Values, Mechanical Properties are at the Peaked Measured Stress State

Depth (ft)	Pressure Range (MPa)	Compressional Wave Velocity (m/s)	Shear Wave Velocity (m/s)		Young's Modulus (GPa)	Poisson's Ratio
			Vs1	Vs2		
2,903	5-70	4,219	2,707	2,614	36.93	0.142
2,903 (p)	10-25	3,930	2,627	2,569	32.87	0.086
2,906	10-25	4,471	2,734	2,855	43.28	0.230
3,024	5-40	5,405	3,392	3,390.	69.47	0.175
3,036	5-70	2,885	1,854	1,877	15.65	0.125
3,179	5-40	5,071	3,191	3,280	61.51	0.166
3,179 (p)	5-60	5,127	3,247	3,221	61.9	0.146
3,188	5-70	2,874	1,779	1,885	15.23	0.148
3,491	5-70	5,449	3,285	3,287	68.36	0.201

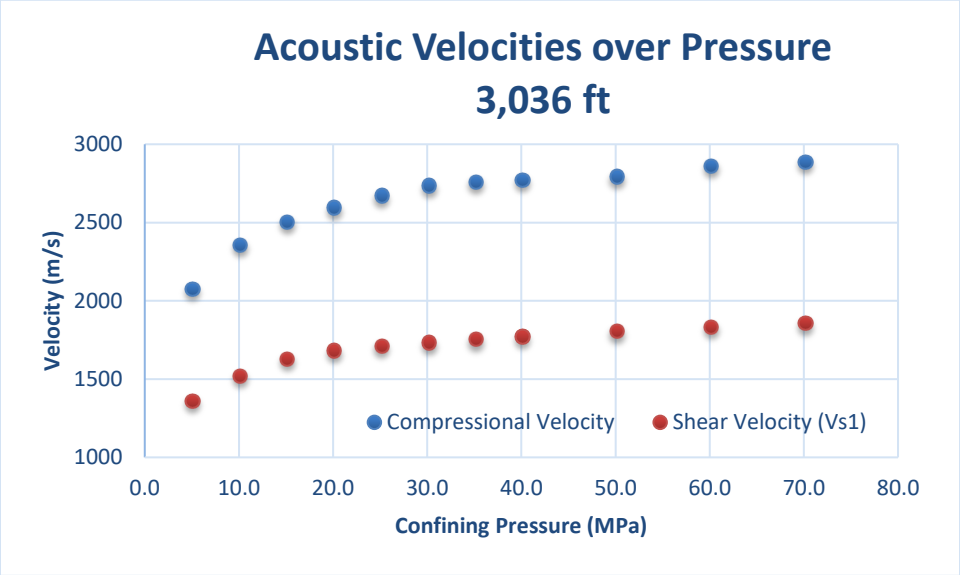

Figure 42: Example of obtained acoustic data for a sample at 3,036 ft.

4. DISCUSSION

The measurements of the magnetic susceptibility, P-wave velocity, XRF, and CT analysis provide a unique look into the internal structure of the core and macroscopic changes in lithology. These techniques:

- Are non-destructive
- When performed in parallel give insight into the core beyond what one individual technique can provide
- Can be used to identify zones of interest for detailed analysis, experimentation, and quantification, for example:
    - Two sandstone zones in the base of the Wabaunsee Group (3,036 ft) and base of the Heebner Formation (3,188 ft.) show high porosity and permeability and likewise have low clay content (Al, Fe, K)
    - Admire Group and upper Wabaunsee Group (2,900 to 3,016 ft) have higher clay contents and low porosity and permeabilities
- Provide a detailed digital record of the core, before any destructive testing or further degradation, that is accessible and can be referenced for future studies

This page intentionally left blank.

5. REFERENCES

Bacon, D. H.; Blankenau, D.; Divine, D.; Duguid, A.; Fukai, I.; Glier, J.; Hawkins, J.; Jimenez, M.; Joeckel, R. M.; McDonald, S.; Middleton, R.; Peterson, R.; Scharenberg, M.; Smith, V.; White, S. K.; Yaw, S. P. *Integrated mid-continent stacked carbon storage hub, Phase I Final Report*; 2018; pp 293. DOI: 10.2172/1478726. https://www.osti.gov/servlets/purl/1478726

Crandall, D.; Moore, J.; Rodriguez, R.; Gill, M.; Soeder, D.; McIntyre, D.; Brown, S. *Characterization of Martinsburg Formation using Computed Tomography and Geophysical Logging Techniques*; NETL-TRS-4-2017; NETL Technical Report Series; U.S. Department of Energy, National Energy Technology Laboratory: Morgantown, WV, 2017; p 68.

Duguid, A. 2017 Integrated Mid-Continent Stacked Carbon Storage Hub, Project DE-FE0029264, Carbon Storage and Oil and Natural Gas Technologies Review Meeting, Pittsburgh PA, August 1-3, 2017.

Geotek Ltd. Geotek Multi-Sensor Core Logger Flyer, Daventry, UK, 2009. http://www.geotek.co.uk/sites/default/files/MSCLOverview.pdf

Geotek Ltd. Multi-Sensor Core Logger Manual; Version 05-10; Published by Geotek, 3 Faraday Close, Daventry, Northamptonshire NN11 8RD, 2010. info@geotek.co.uk, www.geotek.co.uk

Hunts, C.; Moskowitz, B.; Banerjee, S. *Magnetic Properties of Rocks and Minerals;* Rock Physics and Phase Relations: A Handbook of Physical Constants; 1995; p 189-204.

Iowa State University Center for Nondestructive Evaluation, Ames, IA, 2021. https://www.nde-ed.org/Physics/X-Ray/attenuation.xhtml (accessed July 2021).

Johnson, T. R. C. Dual-Energy CT: General Principles. *American Journal of Roentgenology* **2012,** *199*, S3–S8. DOI: 10.2214/AJR.12.9116.Paronish, T.; Mitchell, N.; Schmidt, R.; Moore, J.; Brown, S.; Crandall, D.; Hasiuk, F.; Holubnyak, Y. E. *Computed Tomography Scanning and Geophysical Measurements of the Patterson #5-25 Well in Western Kansas*; DOE/NETL-2022/3737; NETL Technical Report Series; U.S. Department of Energy, National Energy Technology Laboratory: Morgantown, WV, 2022a; p 84. DOI: 10.2172/1896785.

Paronish, T.; Schmitt, R.; Mitchell, N; Brown, S; Crandall, D.; Moore, J.; Hasiuk, F.; Potter, N.; Holubnyak, Y. E. *Computed Tomography Scanning and Geophysical Measurements of the Wellington 1-32 Core*; DOE.NETL-2021.2882; NETL Technical Report Series; U.S. Department of Energy, National Energy Technology Laboratory: Morgantown, WV, 2022b; p 108. DOI: 10.2172/194355.

Schmitt, R.; Paronish, T.; Crandall, D.; Moore, J.; Hasiuk, F.; Potter, N.; Holubnyak, Y. E. *Computed Tomography Scanning and Petrophysical Measurements of the Wellington KGS 2-32 Core*; DOE/NETL-2022/3725; NETL Technical Report Series; U.S. Department of Energy, National Energy Technology Laboratory: Morgantown, WV, 2022; p 60. DOI: 10.2172/1841374.

Schneider, C. A.; Rasband, W. S.; Eliceiri, K. W. NIH Image to ImageJ: 25 years of image analysis. Nature Methods **2012,** *9*, 671-675.

Siddiqui, S.; Khamees, A. A. Dual-Energy CT-Scanning Applications in Rock Characterization. *Society of Petroleum Engineers* **2004**. DOI:10.2118/90520-MS.

Spaulding, R. *Subsurface Experimental Laboratory Autoclave and Core Flow Test Facilities.* 2024, p 2. https://netl.doe.gov/sites/default/files/rdfactsheet/R-D169_5.pdf

Smith, V. L. Reservoir Characterization and Static Earth Modeling for Potential CO_2 Storage in Upper Pennsylvanian Cyclothems of Midcontinent, USA. Graduate Theses, Dissertations, and Problem Reports, 2022, 7593, p 126. https://researchrepository.wvu.edu/etd/7593

Marianne Walck
Director
National Energy Technology Laboratory
U.S. Department of Energy

Mark McKoy
Technology Manager, Advanced Carbon Storage R&D
Science & Technology Strategic Plans and Programs
National Energy Technology Laboratory
U.S. Department of Energy

Darin Damiani
Manager, Carbon Transport and Storage
Office of Fossil Energy and Carbon Management
U.S. Department of Energy

Bryan Morreale
Executive Director
Research and Innovation Center
National Energy Technology Laboratory
U.S. Department of Energy

NETL Technical Report Series